

## An Investigation of Uncertainty Propagation in Non-equilibrium Flows

Tianbai Xiao

To cite this article: Tianbai Xiao (2022) An Investigation of Uncertainty Propagation in Non-equilibrium Flows, International Journal of Computational Fluid Dynamics, 36:4, 294-318, DOI: [10.1080/10618562.2022.2104262](https://doi.org/10.1080/10618562.2022.2104262)

To link to this article: <https://doi.org/10.1080/10618562.2022.2104262>



Published online: 02 Aug 2022.



Submit your article to this journal 



Article views: 74



View related articles 



View Crossmark data 



# An Investigation of Uncertainty Propagation in Non-equilibrium Flows

Tianbai Xiao

Karlsruhe Institute of Technology, Karlsruhe, Germany

## ABSTRACT

Considerable uncertainties can exist between the field solutions of coarse-grained fluid models and the real-world flow physics. To study the emergence, propagation, and evolution of uncertainties poses great opportunities and challenges to develop both sound theories and reliable numerical methods. In this paper, we study the stochastic behaviour of multi-scale gaseous flows from molecular to hydrodynamic level, especially focussing on the non-equilibrium effects. The theoretical analysis is presented based on the gas kinetic model and its upscaling macroscopic system with random inputs. A newly developed stochastic kinetic scheme is employed to conduct numerical simulation of multi-scale and non-equilibrium flows. Different kinds of uncertainties are involved in the gas evolutionary processes. New physical observations, such as the synchronous travel pattern between mean fields and uncertainties, sensitivity of different orders of uncertainties and the influence of boundary effects from continuum to rarefied regimes, are identified and analysed.

## ARTICLE HISTORY

Received 23 November 2021  
Accepted 11 July 2022

## KEYWORDS

Kinetic theory; multi-scale flows; uncertainty quantification; stochastic Galerkin

## 1. Introduction

The study of fluid dynamics is profoundly based on a hierarchy of governing equations at different scales. Counting a great many of fluid elements, the Navier–Stokes equations are the first-principle modelling of conservation laws from a macroscopic perspective. On the other hand, the Boltzmann equation describes the gas dynamic system by tracking the evolution of probabilistic distribution function of single particle. Hilbert's sixth problem (Hilbert 1902) served as an intriguing beginning of trying to describe the behaviour of interacting many-particle systems, including the gas dynamic equations, across different scales. It has been shown since then that some hydrodynamic equations can be derived as the asymptotic limits of kinetic solutions (Grad 1949; Chapman and Cowling 1970).

The theories of fluids can be understood as a coarse-grained approximation of flow physics in the real world. Therefore, considerable uncertainties may be introduced due to the lack of comprehensive knowledge or reduced degrees of freedom in the simplified models. For instance, for the evaluation of collision kernel in the kinetic equations, the phenomenological model parameters often need to be calibrated by

experiments, e.g. the Lennard-Jones molecule model (Lennard-Jones 1924). As a result, the errors inherited from experiments will inevitably influence the numerical evolution of particle interactions at kinetic scale that ought to be deterministic, as well as the reproduced constitutive relationships for the macroscopic moment system.

To evaluate the quality of reduced model and assess the effects of uncertainties on it falls into the topic of uncertainty quantification (UQ). Two fundamental tasks can be related to UQ problems, i.e. the forward and inverse problems. The former pertains to uncertainty propagation from model inputs to outputs where input uncertainties have been characterised stochastically. The latter aims at the parameterisation of uncertainties based on existing data sets. In this paper, we will focus on the forward problem, on which there has been an increasing research interest in computational fluid dynamics (CFD) in recent literature. For example, Cacuci (2003) used local sensitivity analysis and Saltelli, Tarantola, and Chan (1999) adopted moment methods to solve flow problems with relatively small uncertainties. Besides, the spectral methods have been progressively used given the development of polynomial chaos (PC)

methods for the probabilistic representation of uncertainty. Xiu and Karniadakis (2003) discussed the application of generalised polynomial chaos (gPC) to deal with uncertainties with moderate magnitude. Walters and Huyse (2002) analysed these different UQ strategies, and Najm (2009) addressed the usage of PC with the application in compressible flows.

The existing UQ applications of CFD mainly focus on macroscopic fluid dynamic equations with standard stochastic settings. In the recent decades, rapid development has been made in multi-scale algorithms, e.g. the continuum-rarefied hybrid methods (Bourgat, Tallec, and Tidriri 1995; Sun, Boyd, and Candler 2004; Wijesinghe et al. 2004; Degond, Dimarco, and Mieussens 2007) and the asymptotic-preserving (AP) schemes (Lemou and Mieussens 2008; Filbet and Jin 2010; Xu and Huang 2010; Xiao, Cai, and Xu 2017; Xiao 2021a), which has been proved to be an efficient choice to seek the discrete Hilbert's sixth path. However, limited work has been conducted either on the Boltzmann equation in a stochastic sense or on the evolutionary process of uncertainties in multi-scale physics (Hu and Jin 2017; Dimarco and Pareschi 2019). Given the nonlinear system including intermolecular collisions, initial inputs, fluid-surface interactions and geometric complexities, uncertainties may emerge from molecular-level nature, develop upwards, affect macroscopic collective behaviours and vice versa. To study the emergence, propagation and evolution of uncertainty poses great opportunities and challenges to develop both sound theories and reliable multi-scale numerical algorithms.

In this paper, theoretical analysis and numerical experiments will be performed to study the uncertainty propagation in multi-scale and non-equilibrium flows quantitatively. For the theoretical analysis, the kinetic theory of gases is reformulated with the stochastic Galerkin (SG) method, which is an intrusive methodology based on the gPC. The numerical experiments are produced by the newly developed stochastic kinetic scheme (SKS) (Xiao and Frank 2021a, 2021b), which is an efficient method that hybridises intrusive SG and collocation schemes. Several CFD applications, including homogeneous relaxation, normal shock structure and lid-driven cavity, under the different uncertainties from initial flow fields, boundary conditions and intermolecular collision kernels, will be studied in detail.

The rest of this paper is organised as follows. Section 2 is a brief introduction of stochastic kinetic theory and its asymptotic analysis. Section 3 presents a brief introduction of the solution algorithm employed for numerical simulations. Section 4 includes numerical experiments to present and analyse some new physical observations related to uncertainty propagation in fluid dynamics. The last section is the conclusion.

## 2. Stochastic Kinetic Theory of Gases

### 2.1. Boltzmann Equation With Uncertainty

The Boltzmann equation depicts the time-space evolution of particle probability distribution function. In the absence of external force, it can be written as

$$\partial_t f + \mathbf{u} \cdot \nabla_{\mathbf{x}} f = Q(f), \quad (1)$$

where  $f$  is the particle distribution function,  $\mathbf{x} \in D \subseteq \mathbb{R}^3$  is the position in physical space,  $\mathbf{u} \in \mathbb{R}^3$  is the particle velocity and  $Q(f)$  is the collision term. Considering the possible uncertainties in intermolecular collisions, initial and boundary conditions, we can extend the Boltzmann equation with stochastic settings and reformulate the gas kinetic system, i.e.

$$\begin{aligned} \partial_t f + \mathbf{u} \cdot \nabla_{\mathbf{x}} f &= Q(f)(t, \mathbf{x}, \mathbf{u}, \mathbf{z}), \\ t, \mathbf{x}, \mathbf{u}, \mathbf{z} &\in [0, T] \times D \times \mathbb{R}^3 \times I, \\ \mathcal{B}(f)(t, \mathbf{x}, \mathbf{u}, \mathbf{z}) &= 0, \\ t, \mathbf{x}, \mathbf{u}, \mathbf{z} &\in [0, T] \times \partial D \times \mathbb{R}^3 \times I, \\ f(0, \mathbf{x}, \mathbf{u}, \mathbf{z}) &= f_0(\mathbf{x}, \mathbf{u}, \mathbf{z}), \quad \mathbf{x}, \mathbf{u}, \mathbf{z} \in D \times \mathbb{R}^3 \times I, \end{aligned} \quad (2)$$

where  $\mathbf{z} \in I$  is the random variable, and  $\mathcal{B}$  denotes the boundary operator. For brevity, the following analysis will be conducted on basis of the Bhatnagar–Gross–Krook (BGK) model

$$Q(f) = \nu(\mathcal{M} - f), \quad \mathcal{M} = \rho \left( \frac{\lambda}{\pi} \right)^{3/2} e^{-\lambda(\mathbf{u}-\mathbf{U})^2}, \quad (3)$$

where  $\mathcal{M}$  is the Maxwellian distribution function,  $\nu$  is the collision frequency and  $\lambda = m/(2kT)$ , where  $m$  is the particle mass and  $k$  is the Boltzmann constant.

## 2.2. SG Formulation

The methods of UQ can be roughly divided into two subsets, i.e. the intrusive and non-intrusive. The non-intrusive method is basically sampling-based technique. Many realisations of random inputs are generated based on the prescribed probability distribution, for which a deterministic problem is solved. The intrusive methods work in a way such that we reformulate the original deterministic system. It promises an intuitive physical insight and higher-order convergence in the random space. In this part, we introduce the intrusive SG method on basis of the gPC.

Let us consider a gPC expansion of particle distribution function with degree  $N$  in random space, i.e.

$$f(t, \mathbf{x}, \mathbf{u}, \mathbf{z}) \simeq f_N = \sum_{|i|=0}^N \hat{f}_i(t, \mathbf{x}, \mathbf{u}) \Phi_i(\mathbf{z}) = \hat{\mathbf{f}}^T \boldsymbol{\Phi}, \quad (4)$$

where  $i$  could be a scalar or a  $K$ -dimensional vector  $i = (i_1, i_2, \dots, i_K)$  with  $|i| = i_1 + i_2 + \dots + i_K$ . The  $\hat{f}_i$  is the coefficient of  $i$ th PC expansion, and the basis functions used are the normalised orthogonal polynomials  $\{\Phi_i(\mathbf{z})\}$  satisfying the following constraints:

$$\begin{aligned} \mathbb{E}[\Phi_j(\mathbf{z}) \Phi_k(\mathbf{z})] &= \int_{I_z} \Phi_j(\mathbf{z}) \Phi_k(\mathbf{z}) \varrho(\mathbf{z}) d\mathbf{z} \\ &= \delta_{jk}, \quad 0 \leq |j|, |k| \leq N, \end{aligned} \quad (5)$$

where  $\varrho$  is the probability density function. For brevity, we use the notation  $\langle \cdot \rangle$  to denote taking moments along random space henceforth. The expectation value and variance can be evaluated through

$$\begin{aligned} \mathbb{E}(f_N) &= \left\langle \sum_i \hat{f}_i \Phi_i \right\rangle = \hat{f}_0, \\ \text{var}(f_N) &= \left\langle \left( \sum_i \hat{f}_i \Phi_i - \mathbb{E}(f_N) \right)^2 \right\rangle \simeq \sum_{|i|>0} \hat{f}_i^2. \end{aligned} \quad (6)$$

After substituting Equation (4) into the kinetic Equation (2) and performing a Galerkin projection, we then obtain

$$\partial_t \hat{\mathbf{f}} + \mathbf{u} \cdot \nabla_{\mathbf{x}} \hat{\mathbf{f}} = \hat{\mathbf{Q}}, \quad (7)$$

where  $\hat{\mathbf{Q}}$  is the gPC coefficient vector of the projection from collision operator to the polynomial basis. With

the assumption of collision frequency,

$$\nu \simeq \nu_N = \sum_i^N v_i \Phi_i, \quad (8)$$

the collision term in gPC expansion can be written as

$$\begin{aligned} f_N &= \hat{\mathbf{f}}^T \boldsymbol{\Phi} = \sum_i^N \hat{f}_i \Phi_i, \\ \hat{f}_i(f_N) &= \sum_j^N \sum_k^N \hat{v}_j \hat{m}_k \langle \Phi_j \Phi_k, \Phi_i \rangle \\ &\quad - \sum_j^N \sum_k^N \hat{v}_j \hat{f}_k \langle \Phi_j \Phi_k, \Phi_i \rangle, \end{aligned} \quad (9)$$

where  $\hat{m}_k$  is the  $k$ th coefficient in gPC expansion of equilibrium distribution and can be determined by  $\hat{f}$ .

## 2.3. Asymptotic Analysis

The kinetic theory of gases indicates the correspondence between macroscopic and microscopic variables. In the stochastic sense, the macroscopic flow system can also be derived by taking moments along phase space

$$\begin{aligned} \mathbf{W} \simeq \mathbf{W}_N &= \int f_N \varpi d\mathbf{u} = \int \sum_i^N \hat{f}_i(t, \mathbf{x}, \mathbf{u}) \\ &\quad \times \Phi_i(\mathbf{z}) \varpi d\mathbf{u} \\ &= \sum_i^N \left( \int \hat{f}_i \varpi d\mathbf{u} \right) \Phi_i = \sum_i^N \hat{w}_i \Phi_i, \end{aligned} \quad (10)$$

where  $\varpi$  is a vector of velocity moments factors. For conservative flow variables, it holds  $\varpi = (1, \mathbf{u}, \mathbf{u}^2/2)^T$ . In the following, we are going to analyse the current SG BGK equation, with special focus on its asymptotic limiting cases.

### 2.3.1. Homogeneous Case

Let us begin with spatially homogeneous case. In this case, the BGK equation reduces to

$$\partial_t f = \nu(\mathcal{M} - f). \quad (11)$$

It holds the following analytical solution:

$$f = f_0 e^{-\nu t} + \mathcal{M}(1 - e^{-\nu t}), \quad (12)$$

where  $f_0$  is the particle distribution at initial time instant. Given the SG method, we can reformulate the

above solution as

$$f \simeq f_N = \hat{\mathbf{f}}^T \Phi = \sum_i^N \hat{f}_i \Phi_i,$$

$$\hat{f}_i = \left\langle \sum_j^N (\hat{f}_{0j} - \hat{m}_j) \Phi_j \exp \left( - \sum_k^N \hat{v}_k \Phi_k t \right) \Phi_i \right\rangle + \hat{m}_i. \quad (13)$$

Different degrees and kinds of uncertainties can be considered in the above solution.

*Type I.* If the uncertainty comes from stochastic collision frequency  $\nu$  and the initial particle distribution function  $f_0$  is assumed to be deterministic, then according to Equation (10) we have deterministic macroscopic variables and the Maxwellian distribution. Therefore, Equation (13) reduces to

$$\hat{f}_i = \left\langle (f_0 - \mathcal{M}) \exp \left( - \sum_j^N \hat{v}_j \Phi_j t \right) + \mathcal{M}, \Phi_i \right\rangle. \quad (14)$$

The variance of particle distribution function can be approximated by  $\text{var}(f) \simeq \sum_{|i|=1}^N \hat{f}_i^2$ . It is obvious that the variance is zero when  $f_0 = \mathcal{M}$  is a Maxwellian. If  $f_0 \neq \mathcal{M}$ , then the solution becomes stochastic. It can be seen that the variance of solution is zero at either  $t = 0$  or  $t \rightarrow \infty$ , which indicates that an extremum must exist in between. The time to reach the extreme point is determined by the magnitude of  $\nu$ .

Besides, since the collision frequency is independent of particle velocity, it will not affect the shape of particle distribution in velocity space, but plays as a scalar multiplier and only affects thermodynamic properties.

*Type II.* If the uncertainty is imprinted within initial distribution  $f_0$  and the collision kernel is deterministic, Equation (13) becomes

$$\hat{f}_i = \hat{f}_{0i} e^{-\nu t} + \hat{m}_i (1 - e^{-\nu t}). \quad (15)$$

Note that the initial distribution function and the Maxwellian correspond to the same stochastic macroscopic conservative variables in the homogeneous case where transport phenomena are absent, i.e.

$$\hat{w}_i = \left( \int \hat{f}_{0i} \varpi \, d\mathbf{u} \right) = \left( \int \hat{m}_i \varpi \, d\mathbf{u} \right)$$

$$= \left( \int \hat{f}_i \varpi \, d\mathbf{u} \right). \quad (16)$$

Therefore, this case results in long-term and non-vanishing effects of stochasticity. The variation of stochastic solution in magnitude and shape depends on the detailed form of  $f_N$  and  $\mathcal{M}_N$  in particle velocity and probability space.

*Type III.* The last type is a combination of the first two cases. In this case, we need to return to the original Equation (13) without simplification. As can be seen in Equation (13), the gPC coefficients of the expansions in  $f_N$  and  $\nu_N$  are nonlinearly coupled, which makes it difficult to obtain a universal analytical conclusion about the evolution of stochastic solution. A case-by-case analysis must be performed, considering the relative importance of the detailed randomness in the initial solution and the collision kernel. Therefore, we resort to numerical simulations to solve the problems in this case.

### 2.3.2. Inhomogeneous Case

In the spatially inhomogeneous case, if we assume that the collision frequency is a local constant, the formal integral solution of the BGK equation can be written as

$$f(t, \mathbf{x}, \mathbf{u}, \mathbf{z}) = \nu \int_{t_0}^t \mathcal{M}(t', \mathbf{x}', \mathbf{u}, \mathbf{z}) e^{-\nu(t-t')} dt'$$

$$+ e^{-\nu(t-t_0)} f_0(\mathbf{x} - \mathbf{u}(t-t_0), \mathbf{u}, \mathbf{z}), \quad (17)$$

where  $\mathbf{x}' = \mathbf{x} - \mathbf{u}(t-t')$  is the particle trajectory, and  $f_0(\mathbf{x}, \mathbf{u}, \mathbf{z}) = f(t=t_0, \mathbf{x}, \mathbf{u}, \mathbf{z})$  denotes the initial solution.

In the collisionless limit with  $\nu \rightarrow 0$ , the above solution reduces to

$$f(t, \mathbf{x}, \mathbf{u}, \mathbf{z}) = f_0(\mathbf{x} - \mathbf{u}(t-t_0), \mathbf{u}, \mathbf{z}). \quad (18)$$

A Galerkin projection of the above equation results in

$$\hat{f}_i(t, \mathbf{x}, \mathbf{u}) = \hat{f}_{0i}(\mathbf{x} - \mathbf{u}(t-t_0), \mathbf{u}), \quad (19)$$

which indicates that the expectation value  $\hat{f}_{00}$  and the components of variance  $\{\hat{f}_i, 1 \leq |i| \leq N\}$  transport with the same speed  $\mathbf{u}$  in the flow field. In other words, the propagation of the mean and random solution fields in highly rarefied gas is correlated.

In the continuum limit with  $\nu \rightarrow \infty$ , the contribution from the initial value vanishes in Equation (17). We approximate the equilibrium distribution function around  $\{t_0, \mathbf{x}_0\}$  with the first-order Taylor polynomial

$$\mathcal{M}(t, \mathbf{x}, \mathbf{u}, \mathbf{z}) = \mathcal{M}_0(1 + \nabla_{\mathbf{x}} \mathcal{M}_0 \cdot (\mathbf{x} - \mathbf{x}_0))$$

$$+ \partial_t \mathcal{M}_0(t - t_0)), \quad (20)$$

where  $\mathcal{M}_0 = \mathcal{M}(t_0, \mathbf{x}_0, \mathbf{u}, \mathbf{z})$ . Without loss of generality, we can assume  $t_0 = 0$  and  $\mathbf{x}_0 = \mathbf{0}$ , and the integral in Equation (17) becomes

$$\begin{aligned} f(t, \mathbf{x}, \mathbf{u}, \mathbf{z}) &= (1 + \mathbf{x} \cdot \nabla_{\mathbf{x}}) \mathcal{M}_0 + \left( \frac{1}{v} e^{-vt} + te^{-vt} \right) \mathbf{u} \\ &\quad \cdot \nabla_{\mathbf{x}} \mathcal{M}_0 + \left( \frac{1}{v} e^{-vt} + t \right) \partial_t \mathcal{M}_0. \end{aligned} \quad (21)$$

It is obvious that the particle distribution function and collision frequency are nonlinearly coupled. If we further assume  $v$  is deterministic, the above solution reduces to

$$\begin{aligned} \hat{f}_i &= (1 + \mathbf{x} \cdot \nabla_{\mathbf{x}}) \hat{\mathcal{M}}_{0i} + \left( \frac{1}{v} e^{-vt} + te^{-vt} \right) \mathbf{u} \\ &\quad \cdot \nabla_{\mathbf{x}} \hat{\mathcal{M}}_{0i} + \left( \frac{1}{v} e^{-vt} + t \right) \partial_t \hat{\mathcal{M}}_{0i}. \end{aligned} \quad (22)$$

It can be seen that the travel of stochastic solution is constrained by space-time gradients as well as the collision frequency. In other words, diffusion plays a dominant role in the flow evolution. Due to the possible difference in magnitude of different modes in the gPC expansion at different locations, the travel of expectation and propagation of variance can exhibit a certain degree of difference. A typical situation is that the gradients of  $\hat{\mathcal{M}}_0$  and  $\{\hat{\mathcal{M}}_i, |i| \geq 1\}$  are opposite, where the expectation and variance will travel in the opposite direction.

To quantify the correlation between the evolution of expectation and the propagation of variance, we can define the Pearson correlation coefficient, i.e.

$$\mathcal{C} = \frac{\mathbb{E}_{\mathbf{z}}[(\mathbb{E}_{\mathbf{z}}(\beta) - \bar{\mathbb{E}}_{\mathbf{z}}(\beta))(\sigma_{\mathbf{z}}(\beta) - \bar{\sigma}_{\mathbf{z}}(\beta))]}{\sigma_{\mathbf{z}}(\mathbb{E}_{\mathbf{z}}(\beta))\sigma_{\mathbf{z}}(\sigma_{\mathbf{z}}(\beta))}, \quad (23)$$

where  $\{\mathbb{E}_{\mathbf{z}}, \sigma_{\mathbf{z}}\}$  denotes the expectation and standard deviation in random space,  $\{\mathbb{E}_{\mathbf{x}}, \sigma_{\mathbf{x}}\}$  denotes the expectation and standard deviation of inhomogeneous solution in spatial domain,  $\{\bar{\mathbb{E}}_{\mathbf{z}}, \bar{\sigma}_{\mathbf{z}}\}$  denotes the mean value of  $\{\mathbb{E}_{\mathbf{z}}, \sigma_{\mathbf{z}}\}$  over spatial domain, and  $\beta$  is any scalar quantity of interest, e.g. the particle distribution function or a macroscopic variable derived from its velocity moments. The correlation coefficient ranges from  $-1$  to  $1$ . According to the knowledge of statistics (Lee Rodgers and Nicewander 1988), the coefficient  $\mathcal{C}$  is positive if two variables tend to be simultaneously greater than, or simultaneously less than, their respective means, while it is negative if they tend to lie on

opposite sides of their respective means. The stronger is either tendency, the larger is the absolute value of  $\mathcal{C}$ . As two limiting cases, an absolute value of exactly  $1$  implies that a linear equation describes the relationship between two variables perfectly, and a value of  $0$  implies that there is no linear dependency between the variables.

It is noted that the above analysis is performed only in the asymptotic limits of collision frequency  $v$ . As we enter the transition regime, the validity of asymptotic analysis is not guaranteed, and the effects from individual particle transport and intermolecular collision need to be considered uniformly. Therefore, we need to resort to numerical simulation which solves the kinetic equation under stochastic settings. We will employ the criterion in Equation (23) in numerical experiments to check the correlation between expectation and variance field in non-equilibrium flows.

### 2.3.3. Macroscopic Equations

The BGK Equation (1) can be rewritten into the successive form

$$f = \mathcal{M} - \tau Df = \mathcal{M} - \tau D(\mathcal{M} - \tau Df) = \dots, \quad (24)$$

where  $D$  denotes the full derivatives along particle trajectories, and  $\tau = 1/v$  is the mean relaxation time. Truncating the right-hand side at a certain order yields concrete kinetic solution as well as its upscaling moment system, e.g. the Euler with  $O(\tau)$  truncation, Navier–Stokes with  $O(\tau^2)$  truncation, and so on.

Now we look into the SG system. Truncate the solution with zeroth order, i.e.

$$\hat{f} \simeq \hat{\mathbf{m}}, \quad (25)$$

and insert the above solution into Equation (7). The compatibility condition of collision term leads to

$$\int \begin{pmatrix} 1 \\ \mathbf{u} \\ \frac{1}{2} \mathbf{u}^2 \end{pmatrix} (\hat{\mathbf{m}}_t + \mathbf{u} \cdot \nabla_{\mathbf{x}} \hat{\mathbf{m}}) \, d\mathbf{u} = 0, \quad (26)$$

and the corresponding Euler equations yield

$$\frac{\partial}{\partial t} \begin{pmatrix} \hat{\rho} \\ (\hat{\rho} \hat{U}) \\ (\hat{\rho} \hat{E}) \end{pmatrix} + \nabla_{\mathbf{x}} \cdot \begin{pmatrix} \hat{F}_{\rho} \\ \hat{F}_m \\ \hat{F}_e \end{pmatrix} = 0, \quad (27)$$

where  $\{\hat{F}_{\rho}, \hat{F}_m, \hat{F}_e\}$  are the gPC coefficients vector of fluxes for density, momentum and energy. Note that

the above system is not necessarily hyperbolic (Hu and Jin 2017).

For the second-order truncation, the particle distribution in gPC expansion becomes

$$\begin{aligned} f \simeq f_N &= \sum_i^N \hat{f}_i \Phi_i, \\ \hat{f}_i &= \hat{m}_i - \sum_j^N \sum_k^N \hat{\tau}_j (\hat{m}_{kt} + \mathbf{u} \cdot \nabla_{\mathbf{x}} m_k) \langle \Phi_j \Phi_k, \Phi_i \rangle. \end{aligned} \quad (28)$$

Substituting the above solution into Eq. (7), we come to

$$\frac{\partial}{\partial t} \begin{pmatrix} \hat{\rho} \\ (\hat{\rho} \hat{\mathbf{U}}) \\ (\hat{\rho} \hat{\mathbf{E}}) \end{pmatrix} + \nabla_{\mathbf{x}} \cdot \begin{pmatrix} \hat{\mathbf{F}}_\rho \\ \hat{\mathbf{F}}_m \\ \hat{\mathbf{F}}_e \end{pmatrix} = \begin{pmatrix} 0 \\ \hat{\mathbf{S}}_m \\ \hat{\mathbf{S}}_e \end{pmatrix}, \quad (29)$$

where

$$\begin{aligned} \hat{\mathbf{S}}_m &= \int \mathbf{u} \sum_j^N \sum_k^N \hat{\tau}_j (\hat{m}_{kt} + 2\mathbf{u} \cdot \nabla_{\mathbf{x}} m_{kt} \\ &\quad + \mathbf{u} \cdot \nabla_{\mathbf{x}} (\mathbf{u} \cdot \nabla_{\mathbf{x}} m_k)) \\ &\quad \langle \Phi_j \Phi_k, \Phi_i \rangle \varpi \, d\mathbf{u}, \\ \hat{\mathbf{S}}_e &= \int \frac{1}{2} \mathbf{u}^2 \sum_j^N \sum_k^N \hat{\tau}_j (\hat{m}_{kt} \\ &\quad + 2\mathbf{u} \cdot \nabla_{\mathbf{x}} m_{kt} + \mathbf{u} \cdot \nabla_{\mathbf{x}} (\mathbf{u} \cdot \nabla_{\mathbf{x}} m_k)) \\ &\quad \langle \Phi_j \Phi_k, \Phi_i \rangle \varpi \, d\mathbf{u}. \end{aligned} \quad (30)$$

Note that in the deterministic limit, the derivatives of Maxwellian can be evaluated with

$$\begin{aligned} \frac{\partial \hat{m}_0}{\partial t} &= \frac{1}{\hat{\rho}_0} \frac{\partial \hat{\rho}_0}{\partial t} \hat{m}_0 + \frac{3}{2\hat{\lambda}_0} \frac{\partial \hat{\lambda}_0}{\partial t} \hat{m}_0 \\ &\quad + (-\mathbf{u}^2 + 2\mathbf{u} \cdot \hat{\mathbf{U}}_0 - \hat{\mathbf{U}}_0^2) \frac{\partial \hat{\lambda}_0}{\partial t} \hat{m}_0 \\ &\quad + (2\mathbf{u}\lambda - 2\hat{\mathbf{U}}_0\lambda) \cdot \frac{\partial \hat{\mathbf{U}}_0}{\partial t} \hat{m}_0, \\ \nabla_{\mathbf{x}} \hat{m}_0 &= \frac{1}{\hat{\rho}_0} \nabla_{\mathbf{x}} \hat{\rho}_0 \hat{m}_0 + \frac{3}{2\hat{\lambda}_0} \nabla_{\mathbf{x}} \hat{\lambda}_0 \hat{m}_0 \\ &\quad + (-\mathbf{u}^2 + 2\mathbf{u} \cdot \hat{\mathbf{U}}_0 - \hat{\mathbf{U}}_0^2) \nabla_{\mathbf{x}} \hat{\lambda}_0 \hat{m}_0 \\ &\quad + (2\mathbf{u}\hat{\lambda}_0 - 2\hat{\mathbf{U}}_0\hat{\lambda}_0) \cdot \nabla_{\mathbf{x}} \hat{\mathbf{U}}_0 \hat{m}_0, \end{aligned} \quad (31)$$

and Equation (29) reduces to deterministic Navier–Stokes equations

$$\begin{aligned} \frac{\partial}{\partial t} \begin{pmatrix} \hat{\rho}_0 \\ \hat{\rho}_0 \hat{\mathbf{U}}_0 \\ \hat{\rho}_0 \hat{\mathbf{E}}_0 \end{pmatrix} + \nabla_{\mathbf{x}} \cdot \begin{pmatrix} \hat{\rho}_0 \hat{\mathbf{U}}_0 \\ \hat{\rho}_0 \hat{\mathbf{U}}_0 \hat{\mathbf{U}}_0 \\ \hat{\rho}_0 \hat{\mathbf{U}}_0 \hat{\mathbf{E}}_0 \end{pmatrix} \\ = \nabla_{\mathbf{x}} \cdot \begin{pmatrix} 0 \\ \hat{\mathbf{P}}_0 \\ \hat{\mathbf{U}}_0 \cdot \hat{\mathbf{P}}_0 - \hat{\mathbf{q}}_0 \end{pmatrix}. \end{aligned} \quad (32)$$

The stress tensor  $\hat{\mathbf{P}}_0$  and heat flux  $\hat{\mathbf{q}}_0$  are related to particle transport phenomena with non-vanishing mean free path, i.e.

$$\begin{aligned} \hat{\mathbf{P}}_0 &= -\hat{p}_0 \mathbf{I} + \mu \left( \nabla_{\mathbf{x}} \hat{\mathbf{U}}_0 + \nabla_{\mathbf{x}} \hat{\mathbf{U}}_0^T - \frac{2}{3} (\nabla_{\mathbf{x}} \cdot \hat{\mathbf{U}}_0) \mathbf{I} \right), \\ \hat{\mathbf{q}}_0 &= -\kappa \nabla_{\mathbf{x}} \hat{T}_0, \\ \mu &= \tau_0 \hat{p}_0, \quad \kappa = \frac{5}{2} \frac{k}{m} \hat{\tau}_0 \hat{p}_0, \end{aligned} \quad (33)$$

where  $p$  is the thermodynamic pressure,  $\mathbf{I}$  is the identity tensor, and  $k$  is the Boltzmann constant.

### 3. Solution Algorithm

Section 2 corroborates the current stochastic kinetic model in the hydrodynamic limit. However, as we enter the deep end of Knudsen regimes with looser particle interactions, the validity of asymptotic analysis is not guaranteed. The direct numerical modelling and simulation should be employed to investigate the non-equilibrium flow dynamics in conjunction with uncertainty propagation.

In this paper, a newly developed SKS is employed to conduct numerical experiments. The method is a natural extension of the gas kinetic scheme (GKS) (Xu 2001; Xu and Huang 2010) under stochastic settings. In the following, we briefly go through the solution algorithm of the scheme. To avoid tedious repetition, we refer the interested readers to the literature with detailed numerical implementation (Xiao and Frank 2021a).

Within the finite volume framework, the gPC coefficients of particle distribution function in the control volume can be expressed as

$$\hat{f}(t^n, \mathbf{x}_i, \mathbf{u}_j) = \hat{f}_{i,j}^n = \frac{1}{\Omega_i(\mathbf{x}) \Omega_j(\mathbf{u})} \int_{\Omega_i} \int_{\Omega_j} \hat{f}(t^n, \mathbf{x}, \mathbf{u})$$

$$\times d\mathbf{x} d\mathbf{u}, \quad (34)$$

where  $\Omega_i(\mathbf{x})\Omega_j(\mathbf{u})$  are the cell area in the discrete physical and velocity space. The update of particle distribution function is as follows:

$$\begin{aligned} \hat{f}_{i,j}^{n+1} = & \hat{f}_{i,j}^n + \frac{1}{\Omega_i} \int_{t^n}^{t^{n+1}} \sum_{S_r \in \partial\Omega_i} S_r \hat{F}_{r,j}^f dt \\ & + \int_{t^n}^{t^{n+1}} \hat{Q}_{i,j}^f dt, \end{aligned} \quad (35)$$

where  $\hat{F}_r^f$  is the time-dependent fluxes for distribution function at interface  $r$  in physical space,  $S_r$  is the interface area and  $\hat{Q}^f$  is the collision term. Taking velocity moments of Equation (35), we obtain the corresponding macroscopic system

$$\hat{W}_i^{n+1} = \hat{W}_i^n + \frac{1}{\Omega_i} \int_{t^n}^{t^{n+1}} \sum_{S_r \in \partial\Omega_i} S_r \cdot \hat{F}_r^W dt, \quad (36)$$

where  $\hat{F}_r^W$  is the fluxes for conservative variables.

The evaluation of interface flux functions is modelled by the evolving solution of kinetic equation. With a simplified notation of the interface location  $\mathbf{x}_{i+1/2} = 0$  and the initial time instant within a time step  $t^n = 0$ , if we assume the collision frequency as a local constant along physical, velocity and random space, the integral solution of Equation (7) holds along the characteristics

$$\begin{aligned} \hat{f}(t, 0, \mathbf{u}_j) = & v \int_0^t \hat{m}(t', \mathbf{x}', \mathbf{u}_j) e^{-vt'} dt' \\ & + e^{-vt} \hat{f}(0, -\mathbf{u}_j t, \mathbf{u}_j), \end{aligned} \quad (37)$$

where  $\mathbf{x}' = \mathbf{x} - \mathbf{u}t$  is the particle trajectory.

The initial solution of particle distribution  $\hat{f}(0, -\mathbf{u}_j t, \mathbf{u}_j)$  can be obtained through reconstruction technique, e.g.

$$\hat{f}(0, \mathbf{x}, \mathbf{u}_j) = \begin{cases} \hat{f}_{i+1/2,j}^L, & x < 0, \\ \hat{f}_{i+1/2,j}^R, & x \geq 0, \end{cases} \quad (38)$$

with first-order accuracy and

$$\hat{f}(0, \mathbf{x}, \mathbf{u}_j) = \begin{cases} \hat{f}_{i+1/2,j}^L + \partial_{\mathbf{x}} \hat{f}_{i,j} \mathbf{x}, & x < 0, \\ \hat{f}_{i+1/2,j}^R + \partial_{\mathbf{x}} \hat{f}_{i+1,j} \mathbf{x}, & x \geq 0, \end{cases} \quad (39)$$

up to second order, where  $\hat{f}_{i+1/2,j}^{L,R}$  are the reconstructed particle distribution around the interface, and

$\{\partial_{\mathbf{x}} \hat{f}_{i,j}, \partial_{\mathbf{x}} \hat{f}_{i+1,j}\}$  are their slopes in the neighbouring cells.

The macroscopic conservative variables in the gPC expansions at the interface can be evaluated by taking moments over velocity space

$$\hat{\mathbf{w}} = \int_{u_j > 0} \hat{f}_{i+1/2,j}^L \varpi d\mathbf{u}_j + \int_{u_j < 0} \hat{f}_{i+1/2,j}^R \varpi d\mathbf{u}_j, \quad (40)$$

from which the equilibrium distribution function can be defined. The equilibrium distribution around a cell interface can be constructed with respect to desired order of accuracy, e.g. for second-order accuracy

$$\hat{\mathbf{m}}(t, \mathbf{x}, \mathbf{u}) = \hat{\mathbf{m}}^0(1 + \mathbf{a} \cdot \mathbf{x} + At). \quad (41)$$

The space and time derivatives of Maxwellian are related with macroscopic slopes and can be determined with the help of Euler equations

$$\begin{aligned} \frac{\partial \hat{\mathbf{w}}}{\partial t} = & \int A \hat{\mathbf{m}}^0 \varpi d\mathbf{u}, \\ \nabla_{\mathbf{x}} \hat{\mathbf{w}} = & \int \mathbf{a} \hat{\mathbf{m}}^0 \varpi d\mathbf{u}. \end{aligned} \quad (42)$$

After all the coefficients are obtained, the time-dependent interface distribution function can be written as

$$\begin{aligned} f_N(t, 0, \mathbf{u}_j) = & \sum_i^N \hat{f}_i(t, 0, \mathbf{u}_j) = \hat{\mathbf{f}}^T \hat{\Phi}, \\ \hat{\mathbf{f}}(0, t, \mathbf{u}_j) = & (1 - e^{-vt}) \hat{\mathbf{m}}_j^0 \\ & + [(-1 + e^{-vt}) / v + te^{-vt}] \mathbf{u} \cdot \mathbf{a} \hat{\mathbf{m}}_j^0 \\ & + [(vt - 1 + e^{-vt}) / v] A \hat{\mathbf{m}}_j^0 \\ & + e^{-vt} \left[ \left( \hat{f}_{i+1/2,j}^L - \mathbf{u}_j t \partial_{\mathbf{x}} \hat{f}_{i,j} \right) H[\mathbf{u}_j] \right. \\ & \left. + \left( \hat{f}_{i+1/2,j}^R - \mathbf{u}_j t \partial_{\mathbf{x}} \hat{f}_{i+1,j} \right) (1 - H[\mathbf{u}_j]) \right], \end{aligned} \quad (43)$$

where  $H$  is the heaviside step function. The corresponding fluxes of particle distribution function and conservative flow variables can be obtained via

$$\begin{aligned} F_N^f(t, 0, \mathbf{u}_j, \mathbf{z}) = & \mathbf{u}_j f_N(t, 0, \mathbf{u}_j, \mathbf{z}), \\ \mathbf{F}_N^W(t, 0, \mathbf{z}) = & \int \mathbf{u}_j f_N(t, 0, \mathbf{u}_j, \mathbf{z}) \varpi d\mathbf{u}_j, \end{aligned} \quad (44)$$

and the time-integrated fluxes in Equations (35) and (36) can be evaluated with respect to time in Equation (43).

Besides the construction of the interface flux, the collision term needs to be evaluated inside control volume for the update of particle distribution function within each time step. In the solution algorithm, Equation (36) will be updated first, and the obtained macroscopic variables will be used to construct the Maxwellian at  $t^{n+1}$ . As a result, an implicit update of collision term can be achieved based on the explicit solver framework. Let us rewrite the update algorithm for the  $k$ th gPC coefficient of particle distribution function in control volume ( $\Omega_i, \Omega_j$ )

$$\begin{aligned} \hat{f}_{i,j,k}^{n+1} + \Delta t \sum_p^N \sum_q^N \hat{v}_p^{n+1} \hat{f}_q^{n+1} \langle \Phi_p \Phi_q \Phi_k \rangle \\ = \hat{f}_{i,j,k}^n + \frac{1}{\Omega_i} \int_{t^n}^{t^{n+1}} \sum_{S_r \in \partial \Omega_i} S_r \hat{F}_{r,j,k}^f dt \\ + \Delta t \sum_p^N \sum_q^N \hat{v}_p^{n+1} \hat{m}_q^{n+1} \langle \Phi_p \Phi_q \Phi_k \rangle, \end{aligned} \quad (45)$$

which forms a linear system in  $A\hat{f} = B$  manner. The system can be directly solved, but brings considerable computational cost as the gPC expansion order  $N$  increases. It can be solved in a more elegant way with the hybridisation of Galerkin and collocation methods proposed (Xiao and Frank 2021a). The main idea of this method can be summarised as to solve an intrusive SG system with gPC expansions by using collocation points. To make use of it, in the solution algorithm, we first update the gPC macroscopic variables to  $t^{n+1}$  step, and the distribution function to the intermediate step  $t^*$

$$\hat{\mathbf{W}}_{i,k}^{n+1} = \hat{\mathbf{W}}_{i,k}^n + \frac{1}{\Omega_i} \int_{t^n}^{t^{n+1}} \sum_{S_r \in \partial \Omega_i} S_r \cdot \hat{\mathbf{F}}_{r,k}^W dt, \quad (46)$$

$$\hat{f}_{i,j,k}^* = \hat{f}_{i,j,k}^n + \sum_{S_r \in \partial \Omega_i} S_r \hat{F}_{r,j,k}^f dt, \quad (47)$$

which is then evaluated on the quadrature points  $z_q$

$$f_{i,j,q}^* = f_{Ni,j}^*(z_q) = \sum_m^N \hat{f}_{i,j,k}^*(z_q) \Phi_k(z_q). \quad (48)$$

Afterwards, the collision term is solved via

$$\begin{aligned} f_{i,j,q}^{n+1} &= f_{i,j,q}^* + \Delta t v_{i,j,q}^{n+1} (\mathcal{M}_{i,j,q}^{n+1} - f_{i,j,q}^{n+1}) \\ &= (f_{i,j,q}^* + \Delta t v_{i,j,q}^{n+1} \mathcal{M}_{i,j,q}^{n+1}) / (1 + \Delta t v_{i,j,q}^{n+1}). \end{aligned} \quad (49)$$

The updated distribution function can be reabsorbed into the gPC expansion

$$\hat{f}_{i,j,k}^{n+1} = \langle f_{i,j}^{n+1}, \Phi_k \rangle, \quad (50)$$

and the final solution in gPC expansion at  $t^{n+1}$  is

$$f_{Ni,j}^{n+1} = \sum_k^N \hat{f}_{i,j,k}^{n+1} \Phi_k. \quad (51)$$

With the latter hybrid Galerkin-collocation method, the computational efficiency can be improved with orders of magnitude.

#### 4. Numerical Experiments

In this section, we are going to conduct the numerical experiments covering different flow regimes. Different kinds of uncertainties will be coupled with the flow evolving processes throughout the simulations. The motivation of this section, on one hand, is to investigate multi-scale gas dynamic system and analyse typical flow phenomena in conjunction with propagation of uncertainties. On the other hand, it serves to provide the first-hand benchmark solutions of UQ in non-equilibrium flows.

For convenience, dimensionless variables will be introduced in the simulations

$$\begin{aligned} \tilde{\mathbf{x}} &= \frac{\mathbf{x}}{L_0}, & \tilde{\rho} &= \frac{\rho}{\rho_0}, & \tilde{T} &= \frac{T}{T_0}, \\ \tilde{\mathbf{u}} &= \frac{\mathbf{u}}{(2RT_0)^{1/2}}, & \tilde{\mathbf{U}} &= \frac{\mathbf{U}}{(2RT_0)^{1/2}}, \\ \tilde{f} &= \frac{f}{\rho_0(2RT_0)^{3/2}}, & \tilde{\mathbf{T}} &= \frac{\mathbf{T}}{\rho_0(2RT_0)}, \\ \tilde{\mathbf{q}} &= \frac{\mathbf{q}}{\rho_0(2RT_0)^{3/2}}, \end{aligned}$$

where  $R$  is the gas constant,  $\mathbf{T}$  is the stress tensor and  $\mathbf{q}$  is the heat flux. The denominators with subscript zero are characteristic variables in the reference state. For brevity, the tilde notation for dimensionless variables will be removed henceforth.

##### 4.1. Homogeneous Relaxation of Non-equilibrium Distribution

First let us consider the homogeneous relaxation of particles from an initial non-equilibrium distribution.

The evolution system writes

$$f_t = v(\mathcal{M} - f), \quad f(t=0, u) = u^2 e^{-u^2}.$$

The uncertainty originates from collision kernel and results in a stochastic collision frequency  $v \sim \mathcal{N}(1, 0.2^2)$ . It can be written into the gPC expansion

$$v = 1 + 0.2z,$$

where 1 and  $z$  are the first two polynomials in the Hermite system. The theoretical solution can be constructed following the integral solution of homogeneous kinetic model equation. Therefore, the particle distribution function obeys a log-normal distribution in the random space, and the expected value and standard deviation can be constructed as

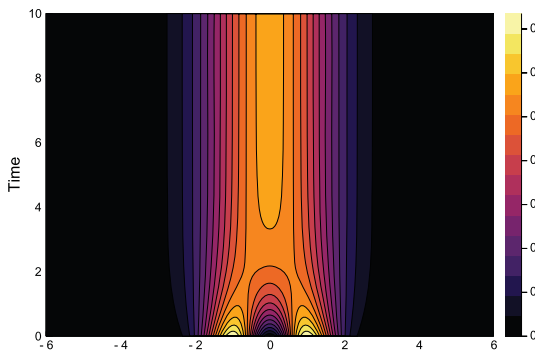
$$\begin{aligned} \mathbb{E}(f) &= f_0 \exp(-t + 0.04t^2/2) \\ &\quad + \mathcal{M}(1 - \exp(-t + 0.04t^2/2)), \\ \mathbb{S}(f) &= [(f_0 - \mathcal{M})^2 (\exp(0.04t^2) - 1) \\ &\quad \times \exp(-2t + 0.04t^2)]^{1/2}. \end{aligned}$$

This case serves as a benchmark validation of the current numerical scheme. The detailed computational setup can be found in Table 1.

The stochastic evolution of particle distribution function in its expectation and standard deviation in the phase space  $\{t \times u\}$  is presented in Figure 1. With

**Table 1.** Computational setup of homogeneous relaxation.

$t$	$\Delta t$	$u$	$N_u$	Integral	$N$
[0, 10]	0.01	[-6, 6]	201	Newton-Cotes	[0, 9]
$N_q$	Polynomial	$v$			
[1, 17]	Hermite	$\mathcal{N}(1, 0.2^2)$			



(a)

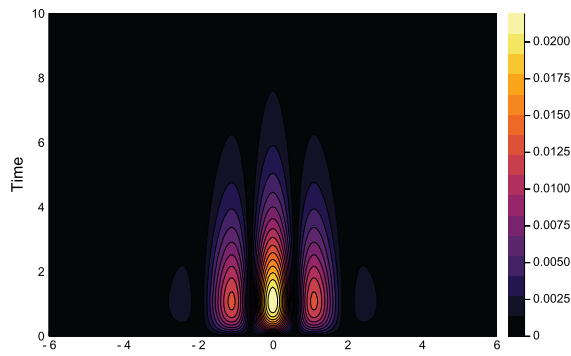
the occurrence of intermolecular interactions, the particle distribution function approaches the Maxwellian gradually from initial bimodal non-equilibrium. A maximal of standard deviation emerges close to the time axis. Such a phenomenon corresponds to the *Type I* stochasticity in Section 2.3.1 and the result matches the theoretical analysis as well as the theoretical solution in Equation (14) perfectly. The evolution process can be understood from a physical point of view. The stochastic collision frequency results in prominent uncertainties only when the intermolecular collision is happening significantly. As time goes with  $t > 8$ , the distribution function gets close to equilibrium state and is thus kept in a dynamical balance with the Maxwellian, which is deterministic in this case. Therefore, the collision term plays no more incentive effects on the propagation of uncertainty.

As the microscopic particle distribution has a one-to-one correspondence with its macroscopic system, we can get the macroscopic evolution by taking moments in the velocity space. Figure 2 presents the time evolution of number density, velocity and temperature. As is shown, the stochastic collision term here plays as a scalar multiplier and only affects gas density.

For the validation of the current scheme, we plot the  $L_1$  and  $L_2$  errors of the numerical solutions with respect to varying order  $N$  for gPC expansions. As is shown, the spectral convergence of the scheme in the probabilistic space is clearly identified (Figure 3).

## 4.2. Normal Shock Structure

In the following, we turn to cases with nonuniform distribution in space. The first example is normal shock



(b)

**Figure 1.** Expectation value and standard deviation of particle distribution within  $\{t, u\} \in [0, 10] \times [-6, 6]$  in the homogeneous relaxation problem: (a) expectation and (b) standard deviation.

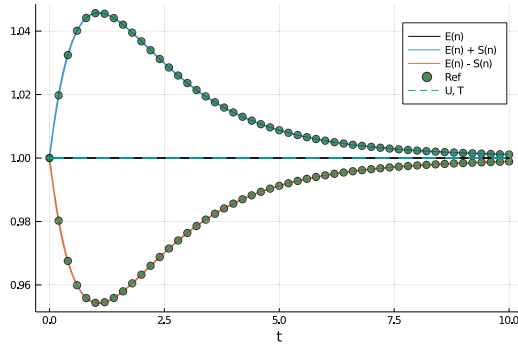


**Figure 2.** Evolution of macroscopic density, velocity and temperature within  $t \in [0, 10]$  in the homogeneous relaxation problem. The results are normalised by the initial values.

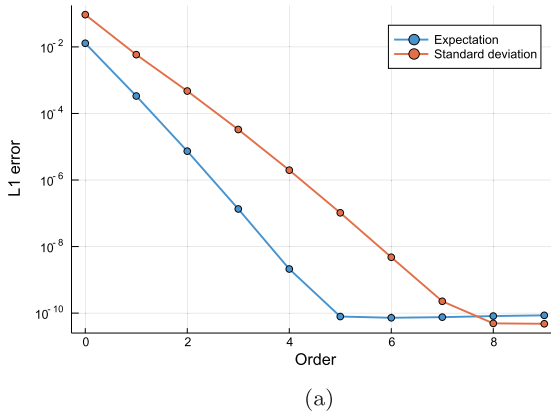
structure, which is highly dissipative and related to strong non-equilibrium effects. Based on the reference frame of shock wave, the stationary upstream and downstream status can be described via the well-known Rankine–Hugoniot relation

$$\begin{aligned}\frac{\rho_+}{\rho_-} &= \frac{(\gamma + 1)Ma^2}{(\gamma - 1)Ma^2 + 2}, \\ \frac{U_+}{U_-} &= \frac{(\gamma - 1)Ma^2 + 2}{(\gamma + 1)Ma^2}, \\ \frac{T_+}{T_-} &= \frac{((\gamma - 1)Ma^2 + 2)(2\gamma Ma^2 - \gamma + 1)}{(\gamma + 1)^2 Ma^2},\end{aligned}$$

where  $\gamma$  is the ratio of specific heat. The upstream and downstream conditions are denoted with  $\{\rho_-, U_-, T_-\}$  and  $\{\rho_+, U_+, T_+\}$ .

The collision frequency in the kinetic equation can be derived from transport phenomena

$$\nu = \frac{p}{\mu},$$



(a)

where  $p$  is the pressure and  $\mu$  is the viscosity coefficient. In this case, we continue dealing with random collision term. A stochastic variable  $\xi$  is introduced in the variable hard-sphere (VHS) model for the evaluation of viscosity, which reads

$$\mu = \xi \mu_0 \left( \frac{T}{T_0} \right)^\eta,$$

and the viscosity coefficient in the reference state is connected with the Knudsen number

$$\mu_0 = \frac{5(\alpha + 1)(\alpha + 2)\sqrt{\pi}}{4\alpha(5 - 2\theta)(7 - 2\theta)} Kn_0,$$

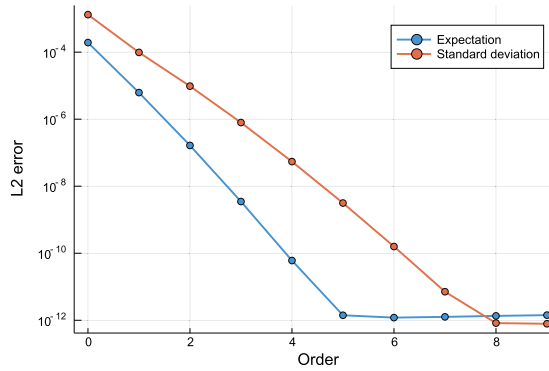
where  $\{\alpha, \theta, \eta\}$  are parameters for the VHS model. The computational setup for this case is presented in Table 2.

The expectations and standard deviations of macroscopic variables at different upstream Mach numbers  $Ma = 2$  and  $3$  are presented in Figures 4 and 5. The solution profiles produced by the discrete velocity method (Xiao 2021b) with 10,000 Monte-Carlo samplings are plotted as reference.

As shown in Figure 5, it is clear that the shock wave serves as a source of uncertainties. The random collision frequency results in the *Type I* stochasticity where significant intermolecular interactions happen, as analysed in Section 2.3.1. Given the fixed Rankine–Hugoniot relationship, the status at the central

**Table 2.** Computational setup of normal shock structure.

$x$ [-35, 35]	$N_x$ 100	$u$ [-12, 12]	$N_u$ 101	Integral Newton-Cotes	$N$ 5
$N_q$ 9	Polynomial Legendre	$\xi$ $\mathcal{U}(0.6, 1.4)$	Ma [2, 3]	Kn 1	CFL 0.5
$\gamma$ 3	$\alpha$ 1	$\theta$ 0.5	$\eta$ 0.81		



(b)

**Figure 3.** Errors of expectation value and standard deviation of particle distribution function within  $\{t, u\} \in [0, 10] \times [-6, 6]$  in the homogeneous relaxation problem: (a)  $L_1$  error and (b)  $L_2$  error.

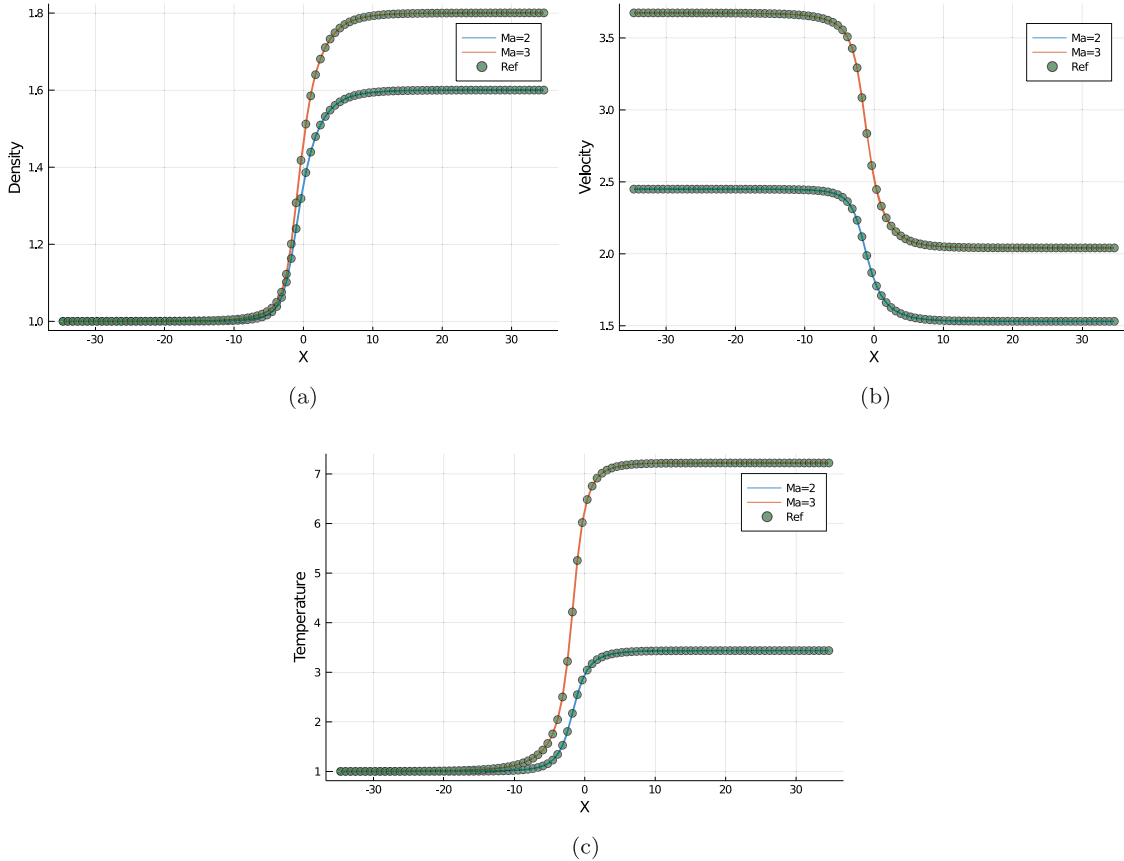


**Figure 4.** Expectation values of macroscopic density, velocity and temperature in the normal shock structure: (a)  $\mathbb{E}(\rho)$ , (b)  $\mathbb{E}(U)$  and (c)  $\mathbb{E}(T)$ .

point of shock  $x = 0$  are directly determined by the upstream and downstream variables. Therefore, the uncertainties of flow field present a bimodal pattern inside the shock profile. In other words, the stochastic collision kernel affects the width and shape of the shock wave structure. Looking into the figures, we can find it seems that the upstream half of shock centre is more sensitive than the downstream part, resulting in a sharper distribution of flow variables. Among all the quantities, the deviation between upstream and downstream of temperature variance is most striking, indicating a higher sensitivity of higher-order moments of particle distribution function.

The gas kinetic modelling and simulation provide us a chance to study the distribution of particles at mesoscopic level. As analysed in Section 2.3, even under the simple viscosity with linear distribution in the random space, Equation (13) promises a cascade evolution mechanism to correlate the gPC expansion coefficients of all orders. Figure 6 presents the gPC

coefficients of particle distribution function at the central point of shock from first order. As can be seen, from the first-order gPC coefficient, the uncertainties are delivered to higher-order moments with descending magnitudes. Counting the contributions from different orders via Equation (6), we get the corresponding expectation and variance of particle distribution function. The higher temperature leads to a wider distribution of particles along velocity space at  $Ma = 3$ . Similar as the profile in physical space, we see the contributions from either side of particle distribution function in velocity space. Three local maximums emerge on the standard deviation profile, which correspond to most probable velocity, and its upstream and downstream (Figure 7).

#### 4.3. Shear Layer

Now let us consider the flow problems in which the transverse processes dominates. A two-dimensional

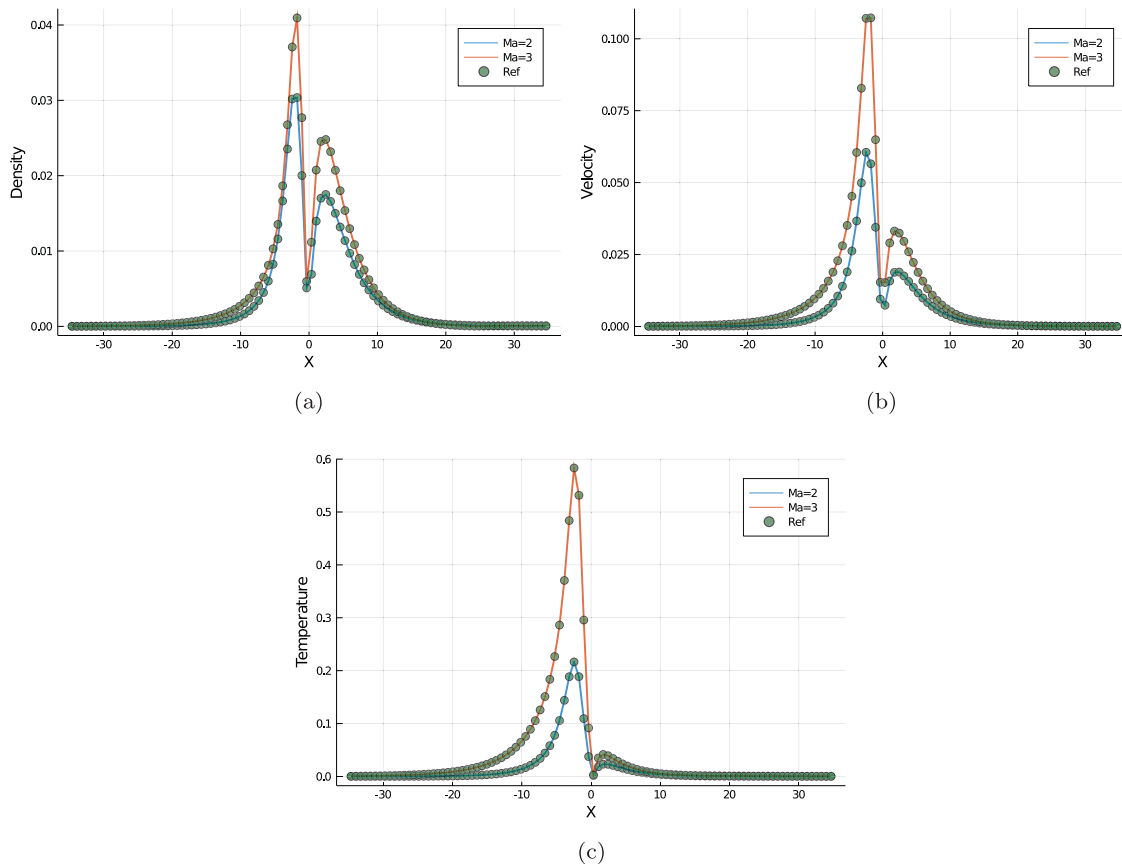


**Figure 5.** Standard deviations of macroscopic density, velocity and temperature in the normal shock structure: (a)  $\mathbb{S}(\rho)$ , (b)  $\mathbb{S}(U)$  and (c)  $\mathbb{S}(T)$ .

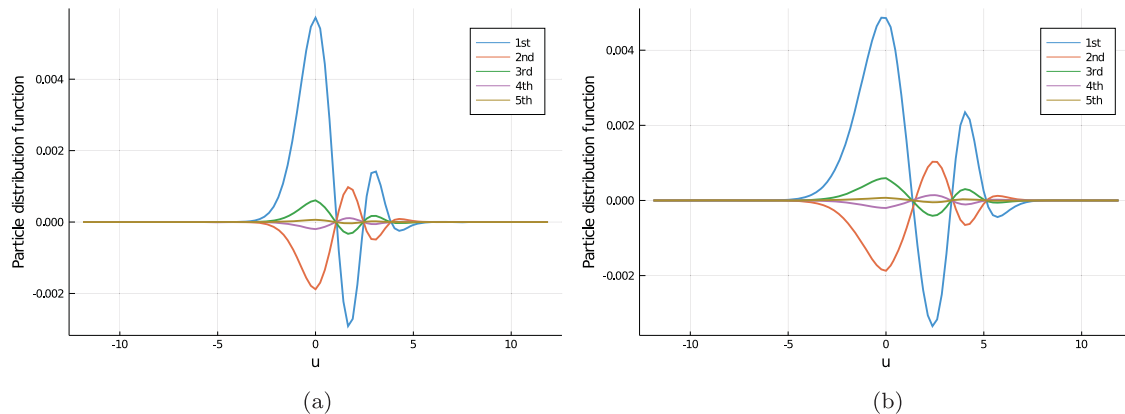


**Figure 6.** PC expansion coefficients of particle distribution function at the centre of normal shock structure: (a)  $Ma = 2$  and (b)  $Ma = 3$ .

shear layer exists in the flow domain, with the initial condition

$$\begin{bmatrix} \rho \\ U \\ V \\ T \end{bmatrix}_L = \begin{bmatrix} 1 \\ 0 \\ \xi \\ 1 \end{bmatrix},$$

$$\begin{bmatrix} \rho \\ U \\ V \\ T \end{bmatrix}_R = \begin{bmatrix} 1 \\ 0 \\ -1 \\ 0.5 \end{bmatrix},$$

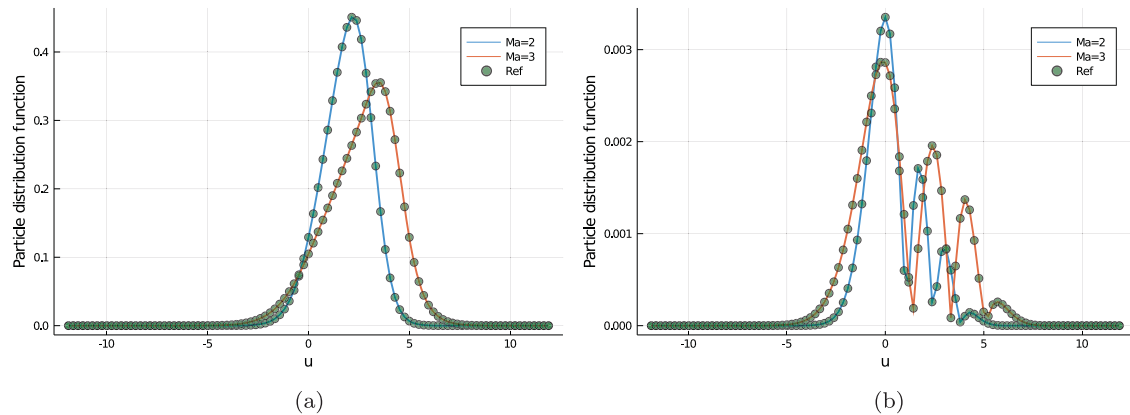


**Figure 7.** Expectation values and standard deviations of particle distribution function at the centre of normal shock structure: (a)  $E(f)$  and (b)  $S(f)$ .

**Table 3.** Computational setup of shear layer.

$t$	$x$	$N_x$	$u$	$N_u$	$v$
$[0, 100\tau_0]$	$[-1, 1]$	1000	$[-4.5, 4.5]$	32	$[-4.5, 4.5]$
$N_v$	Integral	$N$	$N_q$	Polynomial	$\xi$
64	rectangle	5	9	Legendre	$\mathcal{U}(0.9, 1.1)$
$Kn$	CFL	$\gamma$	$\alpha$	$\theta$	$\eta$
0.005	0.5	1.67	1	0.5	0.81

for the right half. The reference viscosity coefficient is evaluated in the same way as described in Section 4.2, and then used to determine the collision time with

$$\tau_0 = \frac{\mu_0}{p_0}.$$

The simulation is conducted within the time period  $t \in [0, 100\tau_0]$ . The computational setup is detailed in Table 3.

Figures 8–10 show the macroscopic flow variables at  $t = \tau_0, 10\tau_0$  and  $100\tau_0$ . Given the pressure difference, the momentum and energy are transferred from left to right. A transition layer is formed that bridges the left and right status of the flow field. As time evolves, the shear layer gradually thickens, in which the transport and diffusion phenomena happen.

The stochastic simulation provides us the opportunity to study the propagation of uncertainties along with the expected bulk flow. From Figures 8–10, we see that the structure of expectation values and standard deviations of flow variables shows a consistent pattern of variation. For example, the profiles of expectation value and standard deviation of V-velocity share similarity in shape, and the higher gradients in the expectation of density and temperature result in larger magnitude in the standard deviation.

To further identify the relevance between the travel of expected flow field and its variance, we check the Pearson correlation coefficient defined in Section 2.3.2. The correlation coefficients of density, velocity and temperature at different time instants are shown in Table 4. It can be seen that the correlation coefficient of V-velocity, which holds the initial random input, stays near the unit value during the flow evolution. Therefore, the correlation between the travel of expected flow field and the propagation of uncertainties are clearly identified. We name such a correspondence as the synchronous travel pattern of expectation and variance. It indicates that the particle transport plays as the dominant mechanism within  $t \in (0, 100\tau_0]$ , of which the effects have been analysed in Section 2.3.2. As the gas dynamic system evolves, the accumulation of intermolecular collisions, i.e. the diffusing effect, leads to a reduction of relevancy of velocity and the increment in density and temperature. Similar as the results in Section 4.2, compared with density and velocity, the temperature distribution is related to the second-order moments of particle distribution function and possesses a higher sensitivity with respect to randomness.

At different time instants, one can find the one-to-one correspondence between the mean flow organisations with their local maximums of variance. The magnitude of variances is positively associated with the gradients of flow variables inside the flow domain. We use the macroscopic equations in Section 2.3.3 to identify the underlying principle semi-quantitatively. For brevity, we take the first-order truncation of the Boltzmann moments system to illustrate the contribution

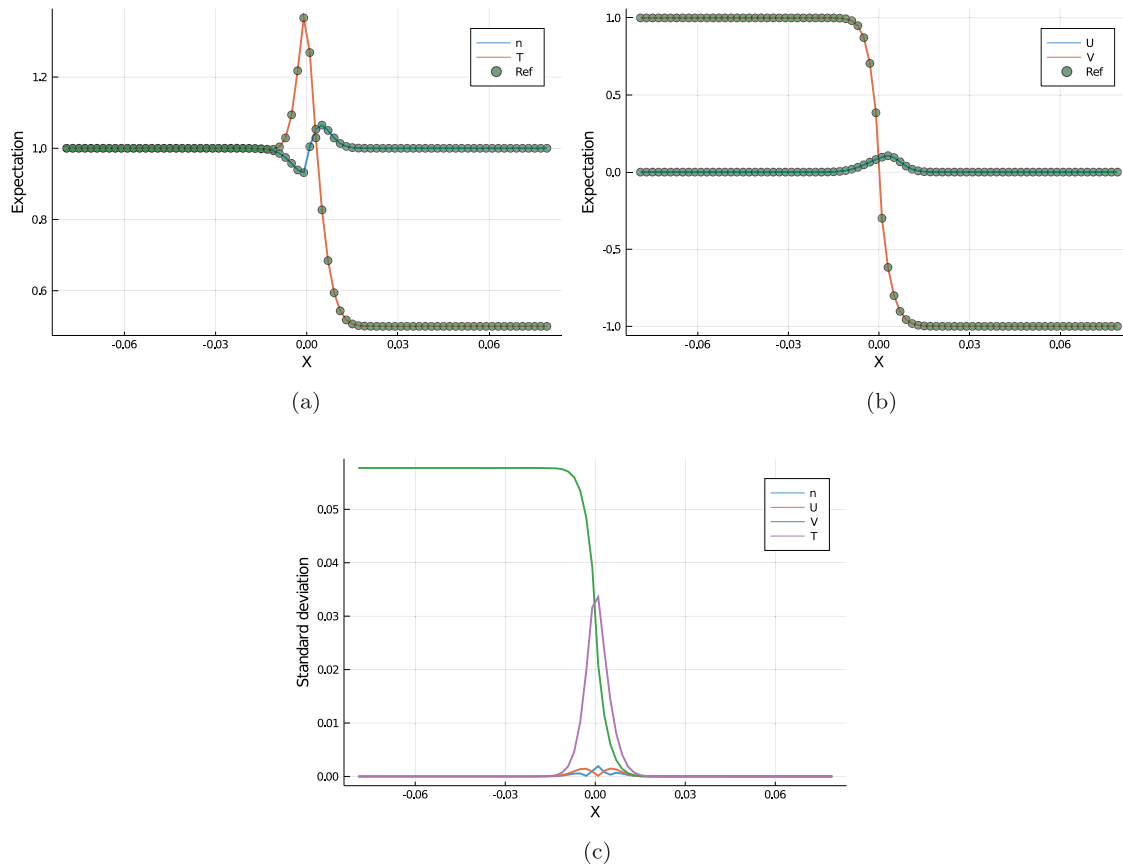


**Figure 8.** Expectation values and standard deviations of macroscopic density, velocity and temperature at  $t = \tau_0$  in the shear layer: (a) expected density and temperature, (b) expected velocity and (c) standard deviation.

of spatial distribution of flow variables onto stochastic evolution. We write down the energy equation in the Navier–Stokes system

$$\partial_t(\rho E) + \nabla_{\mathbf{x}} \cdot (\mathbf{U} \rho E) = -\nabla_{\mathbf{x}} \cdot (\mathbf{P} \cdot \mathbf{U}) - \nabla_{\mathbf{x}} \cdot \mathbf{q},$$

and project it into one-dimensional SG equation, which yields

$$\begin{aligned} \partial_t(\hat{\rho}E)_i + \partial_x \sum_j \sum_k (\hat{\rho}E)_j \hat{U}_k \langle \Phi_j \Phi_k, \Phi_i \rangle \\ = -\partial_x \sum_j \sum_k \left( (\hat{P}_{xx})_j \hat{U}_k + (\hat{P}_{xy})_j \hat{V}_k \right) \\ \langle \Phi_j \Phi_k, \Phi_i \rangle - \partial_x(\hat{q}_x)_i. \end{aligned}$$

We consider the initial status of the shear layer, i.e. the gas is still in the  $x$  direction and only  $V$ -velocity possesses non-zero first-order gPC coefficient  $\hat{V}_1$ . Therefore, the above equation reduces to

$$\begin{aligned} \partial_t(\hat{\rho}E)_i = -\partial_x \sum_j \sum_k \left( (\hat{P}_{xy})_j \hat{V}_k \right) \langle \Phi_j \Phi_k, \Phi_i \rangle \\ - \partial_x(\hat{q}_x)_i, \end{aligned}$$

where the  $j$ th gPC component of stress  $P_{xy}$  is

$$(\hat{P}_{xy})_j = \int \sum_p \sum_q u(v - \hat{V}_p) \hat{f}_q \langle \Phi_p \Phi_q, \Phi_j \rangle du dv.$$

Therefore, the discontinuous distribution of first-order gPC coefficients for  $V$ -velocity results in a nonlinear increase at the same order of energy, which turns the initial deterministic temperature into stochastic one. It also explains the sensitivity of temperature with respect to randomness since such a nonlinear correlation is absent in mass and momentum equations.

The particle distribution function along  $v$ -velocity at the domain centre  $x = 0$  is shown in Figure 11. Over time, the particle distribution function evolves from initial non-equilibrium bimodal distribution towards Maxwellian, resulting in moderate profiles of conservative variables. Similar as macroscopic variables, the clear upstream and downstream effects can be observed in the standard deviations of particle distribution function, where each contributes a major source for randomness. During the gas evolutionary

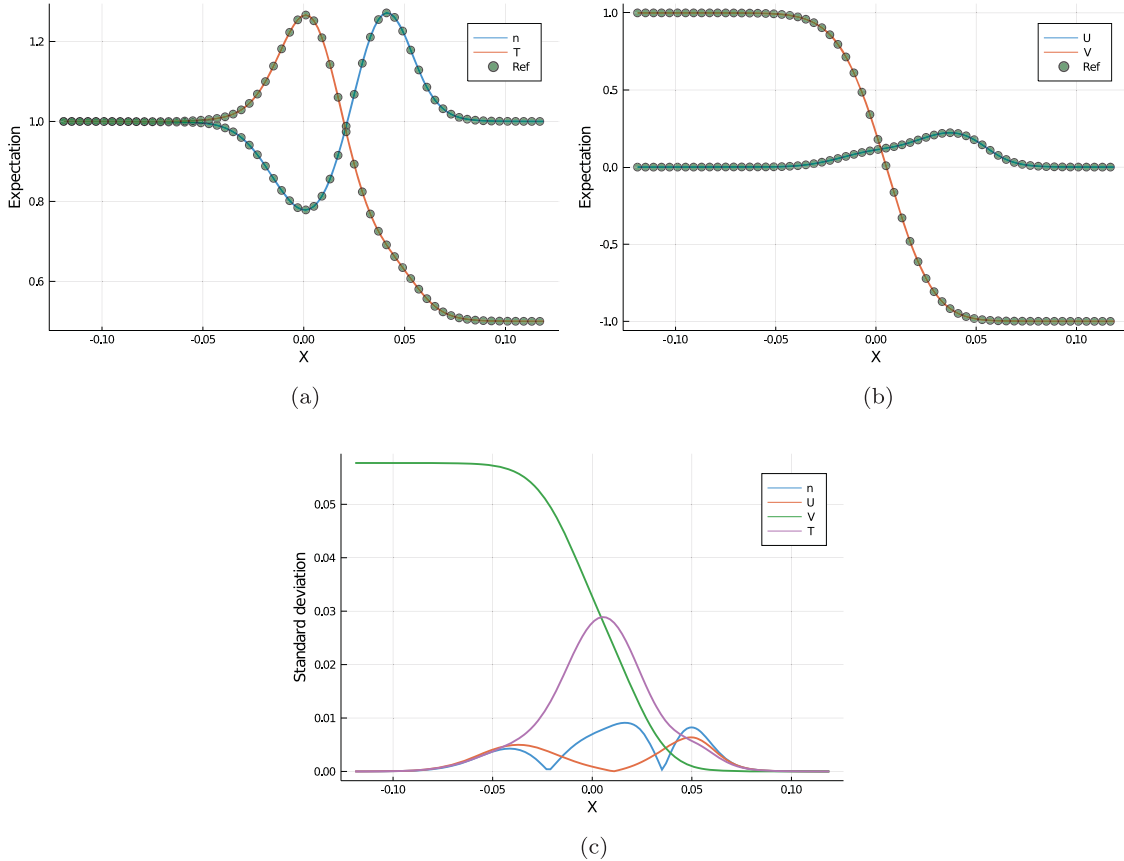


**Figure 9.** Expectation values and standard deviations of macroscopic density, velocity and temperature at  $t = 10\tau_0$  in the shear layer: (a) expected density and temperature, (b) expected velocity and (c) standard deviation.

process, the magnitudes of variances are persistently amplified.

#### 4.4. Lid-Driven Cavity

The lid-driven cavity is a complex system under the synergy of boundary effect, shearing process, swirling flow and heat transfer. In the simulation, the gas is enclosed by four solid walls, while the upper wall is moving in the transverse direction with  $\{U_w = \xi, V_w = 0\}$ . The Maxwell boundary condition is adopted for all the walls, and thus the boundary distribution function for flux evaluation is constructed as follows:

$$f_w = \mathcal{M}_w H(\mathbf{u} \cdot \mathbf{n}) + f_{in} (1 - H(\mathbf{u} \cdot \mathbf{n})), \quad (52)$$

where  $\mathcal{M}_w$  is the Maxwellian at solid wall,  $f_{in}$  is the distribution function extrapolated from inner flow field,  $\mathbf{n}$  is the unit direction vector of boundary and  $H(x)$  is the heaviside step function. The detailed computational setup is listed in Table 5.

In this case, the movement of upper surface is the source for the inner fluid motion. The non-equilibrium shearing transfers vorticity downwards and helps form the eddies inside the cavity. Figure 12 presents expectation values and standard deviations of  $U$ -velocity contours along with velocity vectors. As is shown, a steady main vortex is formed in all cases with different Knudsen numbers in the reference state. At  $Kn = 0.001$  two small corner vortices exist along with the main eddy, while then disappears as  $Kn$  increases. The results here are consistent with the solutions shown in the literature (Xiao et al. 2018).

Figure 12(d) and (e) shows the standard deviations of  $U$ -velocity inside the cavity. The results show that the upper boundary and main vortex are two main sources of uncertainty. As shown in Equation (52), the stochastic wall speed defines the Maxwellian distribution at the boundary and then participates in the flux evolution. Due to the slip effect in the gas-surface interaction, the magnitude of velocity magnitude as well as its variance decreases persistently with the increasing Knudsen number. Figures 13 and 14

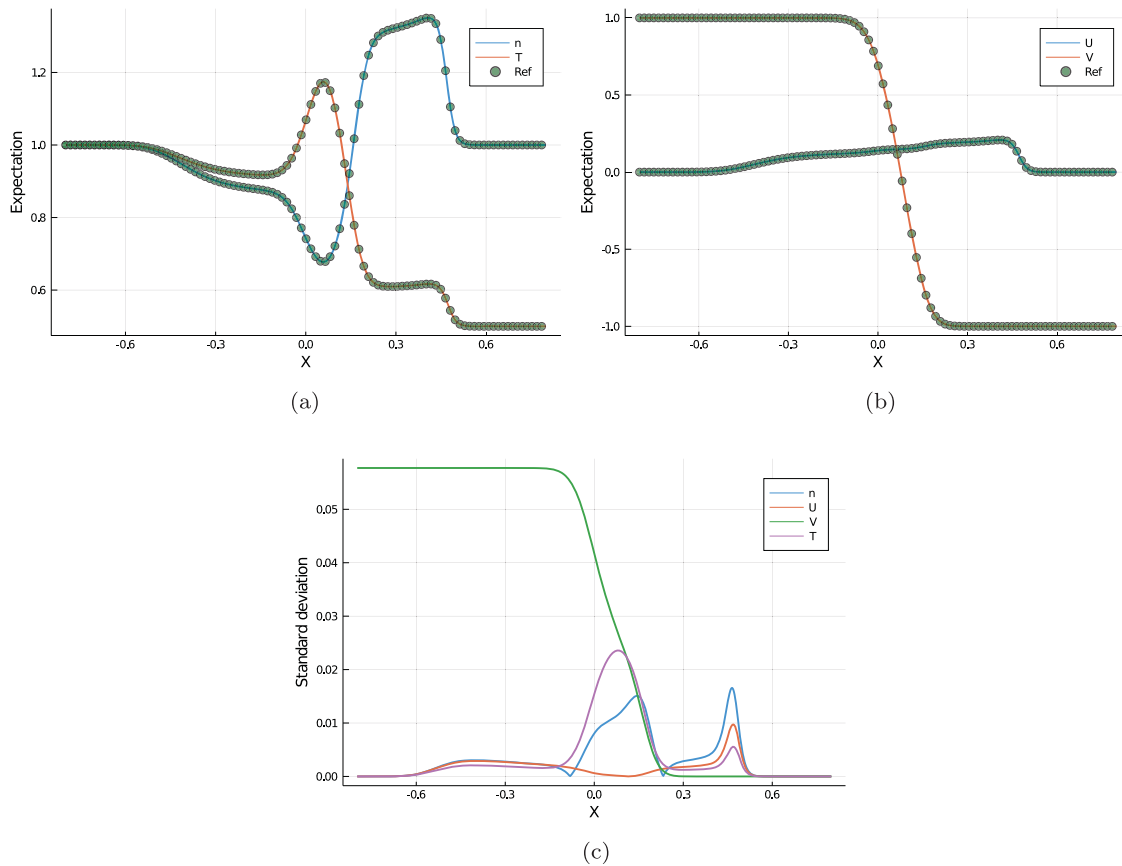


**Figure 10.** Expectation values and standard deviations of macroscopic density, velocity and temperature at  $t = 100\tau_0$  in the shear layer: (a) expected density and temperature, (b) expected velocity and (c) standard deviation.

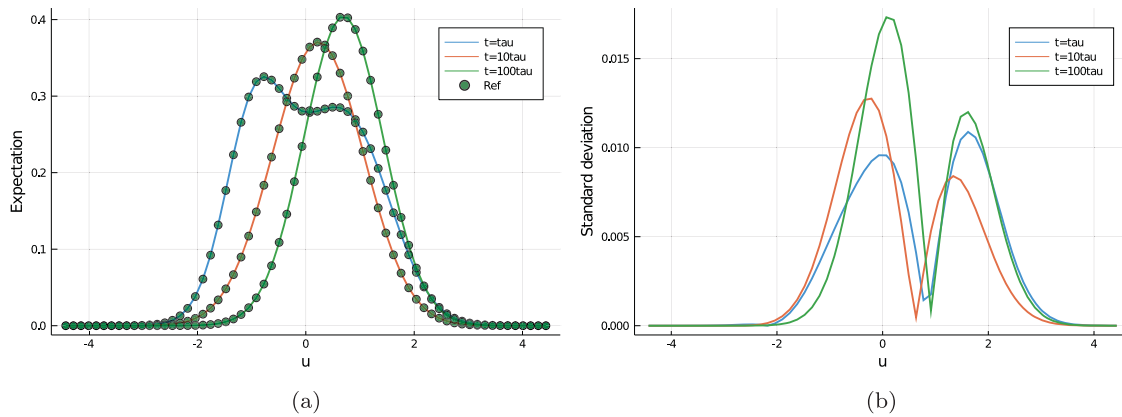


**Figure 11.** Expectation values and standard deviations of particle distribution function at the domain centre  $x = 0$ : (a) expectation value and (b) standard deviation.

provide the velocity distributions along the vertical ( $x = 0.5$ ) and horizontal ( $y = 0.5$ ) centre lines. With the increasing  $Kn$ , the intensity of vortex is damped by the enhanced viscosity, resulting in milder distribution along the centre lines. From Figure 13, we clearly see the slip effect at boundary in the transition regime

of flow dynamics, and its influence on the expected velocity profile and its variance.

For a better understanding of the transverse process of flow dynamics inside the cavity, the distributions of vorticity  $\omega = \partial_x V - \partial_y U$ , are plotted in Figure 15. Due to the fact that the main eddy (similar as point

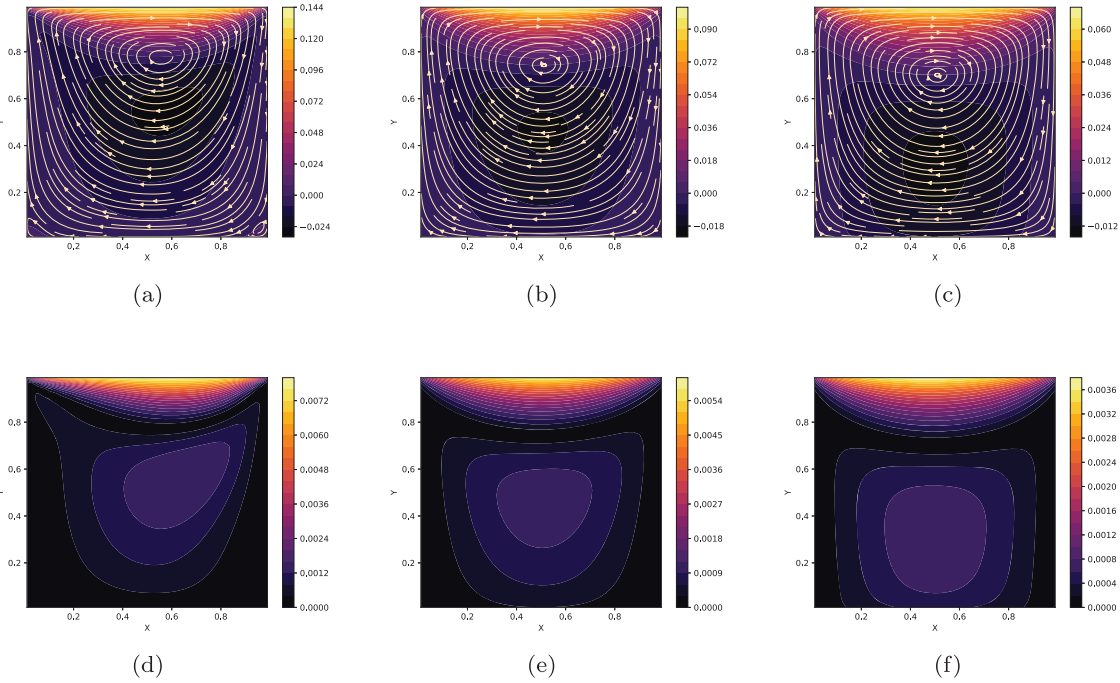


**Figure 12.** Expectation values (first row) and standard deviations (second row) of  $U$ -velocity (contour) and streamline (vector) at different reference Knudsen numbers in the lid-driven cavity: (a)  $\text{Kn} = 0.001$ , (b)  $\text{Kn} = 0.075$ , (c)  $\text{Kn} = 0.5$ , (d)  $\text{Kn} = 0.001$ , (e)  $\text{Kn} = 0.075$  and (f)  $\text{Kn} = 0.5$ .

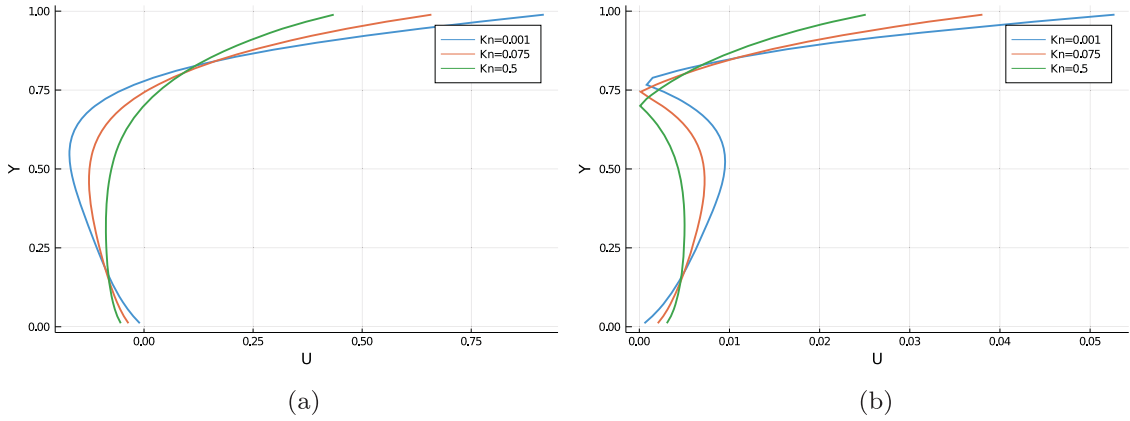


**Figure 13.** Expectation values (left) and standard deviations (right) of  $U$ -velocity along the vertical centre line  $x = 0.5$  at different reference Knudsen numbers in the lid-driven cavity. The velocities have been normalised by  $U_w$ : (a)  $\mathbb{E}(U)$  and (b)  $\mathbb{S}(U)$ .

**Table 4.** Correlation coefficients of expectation values and standard deviations of different variables at different time instants in the shear layer.

	$\rho$	$U$	$V$	$T$
$t = \tau_0$	0.002	0.837	1	0.125
$t = 10\tau_0$	0.016	0.632	1	0.237
$t = 100\tau_0$	-0.105	0.425	0.997	0.370

vortex) contributes negligible vorticity, the shearing process near four boundaries plays a major role in vorticity transport. Obviously, the slip effect also has significant influence on the magnitude of boundary vorticity flux. The strength of vorticity transport as

**Table 5.** Computational setup of lid-driven cavity.

$x$ [0, 1]	$y$ [0, 1]	$N_x$ 45	$N_y$ 45	$u$ [-5, 5]	$N_u$ 60
$v$ $N_v$		Integral	$N$	$N_q$	Polynomial
$[-5, 5]$	60	rectangle	4	7	Legendre
$\xi$ $Kn$		CFL	$\gamma$	$\alpha$	$\theta$
$\mathcal{U}(0.9, 1.1)$	[0.001, 0.1]	0.8	1.67	1	0.5
$\eta$	Boundary				
0.72	Maxwell				

well as its variance decreases in correspondence with the increasing Knudsen number.

The heat transfer inside cavity is crossly coupled with flow transport. Figure 16 shows the expectation

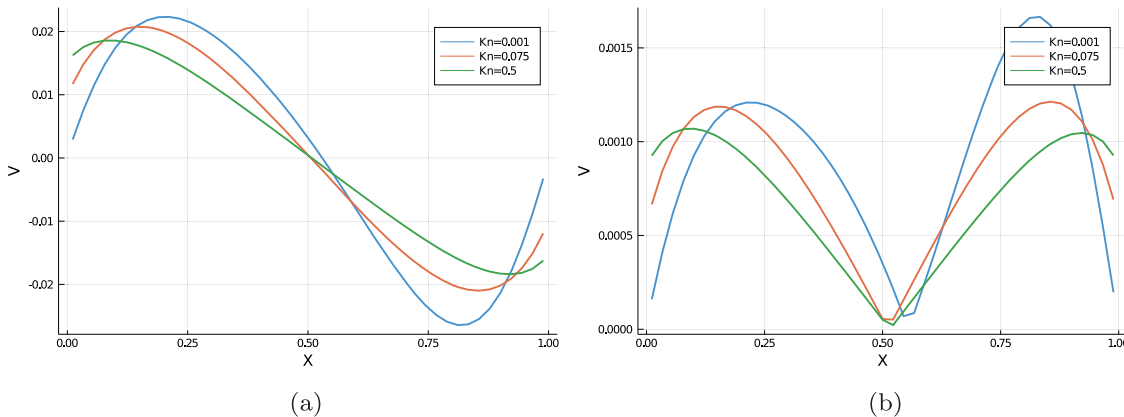


**Figure 14.** Expectation values (left) and standard deviations (right) of  $V$ -velocity along the horizontal centre line  $y = 0.5$  at different reference Knudsen numbers in the lid-driven cavity. The velocities have been normalised by  $U_w$ : (a)  $\mathbb{E}(V)$  and (b)  $\mathbb{S}(V)$ .

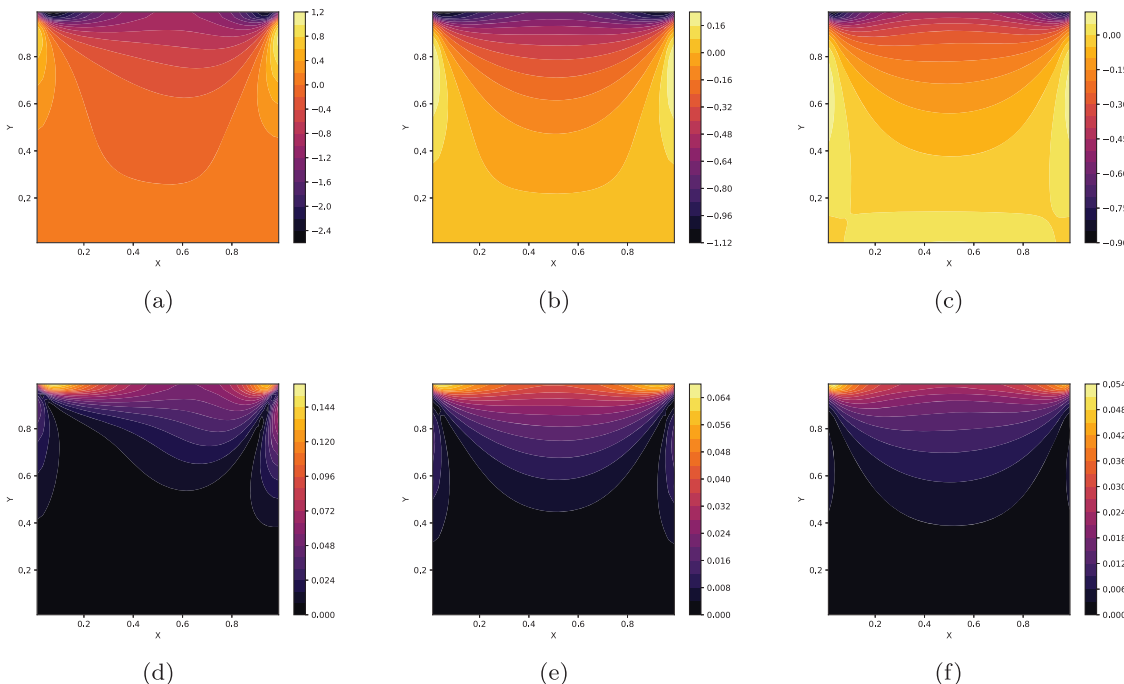


**Figure 15.** Expectation values (first row) and standard deviations (second row) of vorticity at different reference Knudsen numbers in the lid-driven cavity: (a)  $Kn = 0.001$ , (b)  $Kn = 0.075$ , (c)  $Kn = 0.5$ , (d)  $Kn = 0.001$ , (e)  $Kn = 0.075$  and (f)  $Kn = 0.5$ .

values and standard deviations of temperature contours along with heat flux vectors. As demonstrated, the viscous heating at the top right corner contribute one local maximum of temperature. Meanwhile, the loose coupling among particles leads to an expansion cooling effect around the top left, and results in a minimum in the transition regime. With the increasing Knudsen number, the heat flux gradually deviates from the Fourier's law, and the heat transports from the cold to hot region. Such an anti-gradient heat flux is induced by viscous shearing, which is a typical non-equilibrium phenomenon in the cavity flow.

Figure 16(d) and (e) shows the standard deviations of temperature. Compared with the transport of expected fields, the propagation of temperature variances presents a semblable distribution, i.e. the synchronous travel pattern. To illustrate the relevance between the travel of expected flow field and its variance, we provide the Pearson correlation coefficient defined in Section 2.3.2 of density, velocity, temperature, heat flux and vorticity in Table 6. The correlation between the travel of expected flow field and the propagation of uncertainties is clearly identified. While the  $U$ -velocity which accepts the boundary random

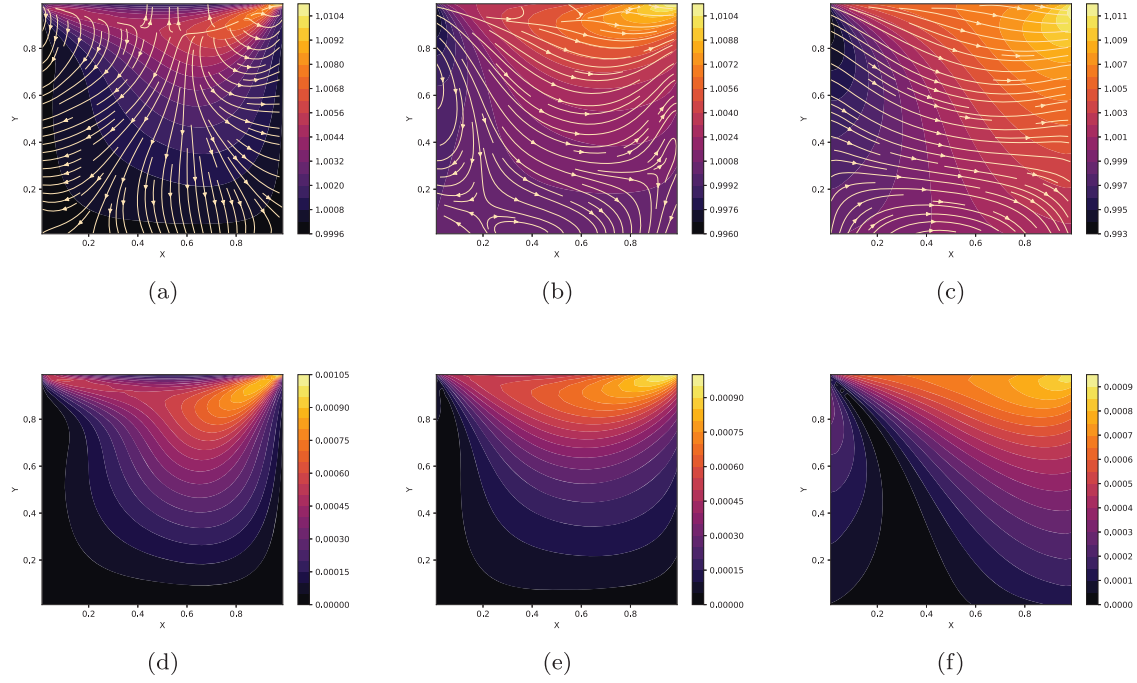


**Figure 16.** Expectation values (first row) and standard deviations (second row) of temperature (contour) and heat flux (vector) at different reference Knudsen numbers in the lid-driven cavity: (a)  $Kn = 0.001$ , (b)  $Kn = 0.075$ , (c)  $Kn = 0.5$ , (d)  $Kn = 0.001$ , (e)  $Kn = 0.075$  and (f)  $Kn = 0.5$ .

input is basically consistent, the correlation of vorticity as well as thermodynamic quantities strengthens with the increasing Knudsen number. It can be understood that as  $Kn$  increases, the loose coupling of particles enhances the freedom of transport phenomena, and the corner-effect zones from two vertices enlarge downwards. The influence of main eddy decreases with increasing dissipation and the energy transport inside cavity presents the tendency with enhanced horizontal characteristics. Figure 17 presents the distribution of components of heat flux and their standard deviations. In spite of the synchronous travelling between the mean field and its variance, it should be noticed that such a correspondence does not necessarily happen one by one. For example, at  $Kn = 0.5$  the upper half of right side wall with high value of  $\mathbb{E}(q_y)$  does not hold  $\mathbb{S}(q_y)$  maximum routinely as it is at  $Kn = 0.075$ . The standard deviation does not vary monotonically with respect to the Knudsen number, but could hold a maximum at a certain point in the transition regime. It can be inferred that peculiarity exists for higher-order velocity moments of particle distribution function, which is more sensitive to the slight change of distribution function and its variance.

**Table 6.** Correlation coefficients of expectation values and standard deviations of different variables at different reference Knudsen numbers in the lid-driven cavity.

	$\rho$	$U$	$V$	$T$	$q_x$	$q_y$	$\omega$
$Kn = 0.001$	0.127	0.848	-0.129	0.995	0.855	0.292	-0.876
$Kn = 0.075$	0.072	0.843	0.051	0.962	0.848	-0.522	-0.948
$Kn = 0.5$	0.1434	0.845	0.108	0.846	0.963	-0.888	-0.981

## 5. Conclusion

As the CFD plays a more important role in the study on flow mechanism and spacecraft design, deterministic theoretical and numerical solutions may not be taken for granted. In this paper, a general methodology of modelling and simulating multi-scale flow dynamics is proposed in conjunction with uncertain quantification. The Boltzmann model equation is reformulated with the SG method, and theoretical analysis is presented quantitatively in both kinetic regime and its upscaling macroscopic moments system. A newly developed SKS is employed for numerical investigations with full validations. Different numerical experiments, including homogeneous relaxation of particle distribution function, normal shock wave structure, transient shear layer and lid-driven cavity in different

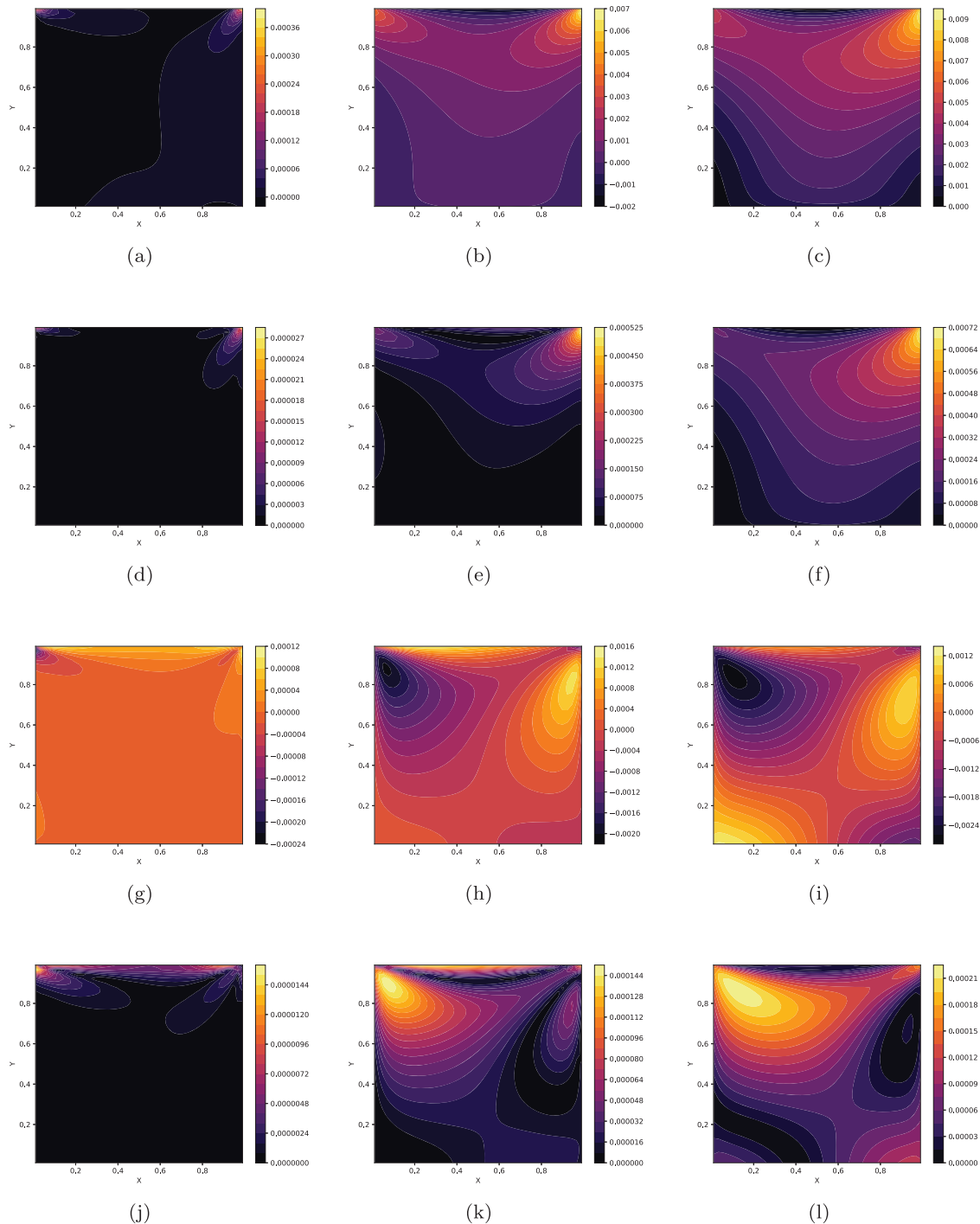


**Figure 17.** Expectation values and standard deviations of heat flux at different reference Knudsen numbers in the lid-driven cavity. The four rows are  $\mathbb{E}(q_x)$ ,  $\mathbb{S}(q_x)$ ,  $\mathbb{E}(q_y)$  and  $\mathbb{S}(q_y)$ , respectively: (a)  $Kn = 0.001$ , (b)  $Kn = 0.075$ , (c)  $Kn = 0.5$ , (d)  $Kn = 0.001$ , (e)  $Kn = 0.075$ , (f)  $Kn = 0.5$ , (g)  $Kn = 0.001$ , (h)  $Kn = 0.075$ , (i)  $Kn = 0.5$ , (j)  $Kn = 0.001$ , (k)  $Kn = 0.075$  and (l)  $Kn = 0.5$ .

flow regimes, are studied subject to different kinds of uncertainties from initial status, boundary conditions and intermolecular collision kernels. Favorable agreements are achieved between theoretical analysis and numerical results. New physical phenomena, such as the consistent propagating patterns of mean fields and uncertainties from continuum to rarefied

regimes, are observed and analysed systematically. The current method provides an innovative tool for sensitivity analysis, flow diagnoses and optimisation for the study of CFD, especially on non-equilibrium flow dynamics. Confined to the computational resources, multi-dimensional uncertainties in probabilistic space will be further considered in future work.

## Disclosure statement

No potential conflict of interest was reported by the author.

## References

- Bourgat, Jean-François, Patrick Le Tallec, and Moulay D. Tidiriri. 1995. "Coupling Boltzmann and Navier–Stokes Equations by Friction." *Journal of Computational Physics* 127 (2): 227–245.
- Cacuci, Dan G. 2003. *Sensitivity and Uncertainty Analysis, Volume I: Theory*. Boca Raton: Chapman & Hall/CRC.
- Chapman, Sydney, and Thomas George Cowling. 1970. *The Mathematical Theory of Non-uniform Gases: An Account of the Kinetic Theory of Viscosity, Thermal Conduction and Diffusion in Gases*. New York: Cambridge University Press.
- Degond, Pierre, Giacomo Dimarco, and Luc Mieussens. 2007. "A Moving Interface Method for Dynamic Kinetic–Fluid Coupling." *Journal of Computational Physics* 227 (2): 1176–1208.
- Dimarco, Giacomo, and Lorenzo Pareschi. 2019. "Multi-scale Control Variate Methods for Uncertainty Quantification in Kinetic Equations." *Journal of Computational Physics* 388: 63–89.
- Filbet, Francis, and Shi Jin. 2010. "A Class of Asymptotic-preserving Schemes for Kinetic Equations and Related Problems with Stiff Sources." *Journal of Computational Physics* 229 (20): 7625–7648.
- Grad, Harold. 1949. "On the Kinetic Theory of Rarefied Gases." *Communications on Pure and Applied Mathematics* 2 (4): 331–407.
- Hilbert, David. 1902. "Mathematical Problems." *Bulletin of the American Mathematical Society* 8 (10): 437–479.
- Hu, Jingwei, and Shi Jin. 2017. "Uncertainty Quantification for Kinetic Equations." In *Uncertainty Quantification for Hyperbolic and Kinetic Equations*, 193–229. Cham: Springer.
- Lee Rodgers, Joseph, and W. Alan Nicewander. 1988. "Thirteen Ways to Look at the Correlation Coefficient." *The American Statistician* 42 (1): 59–66.
- Lemou, Mohammed, and Luc Mieussens. 2008. "A New Asymptotic Preserving Scheme Based on Micro–Macro Formulation for Linear Kinetic Equations in the Diffusion Limit." *SIAM Journal on Scientific Computing* 31 (1): 334–368.
- Lennard-Jones, John Edward. 1924. "On the Determination of Molecular Fields. II. From the Equation of State of Gas." *Proceedings of the Royal Society of London. Series A* 106: 463–477.
- Najm, Habib N. 2009. "Uncertainty Quantification and Polynomial Chaos Techniques in Computational Fluid Dynamics." *Annual Review of Fluid Mechanics* 41: 35–52.
- Saltelli, Andrea, Stefano Tarantola, and K. P.-S. Chan. 1999. "A Quantitative Model-Independent Method for Global Sensitivity Analysis of Model Output." *Technometrics* 41 (1): 39–56.
- Sun, Quanhua, Iain D. Boyd, and Graham V. Candler. 2004. "A Hybrid Continuum/Particle Approach for Modeling Subsonic, Rarefied Gas Flows." *Journal of Computational Physics* 194 (1): 256–277.
- Walters, Robert W., and Luc Huyse. 2002. "Uncertainty Analysis for Fluid Mechanics with Applications." Technical Report. National Aeronautics and Space Administration Hampton VA Langley Research Center.
- Wijesinghe, H. S., R. D. Hornung, A. L. Garcia, and N. G. Hadjiconstantinou. 2004. "Three-dimensional Hybrid Continuum-Atomistic Simulations for Multiscale Hydrodynamics." *Journal of Fluids Engineering* 126 (5): 768–777.
- Xiao, Tianbai. 2021a. "A Flux Reconstruction Kinetic Scheme for the Boltzmann Equation." *Journal of Computational Physics* 447: 110689.
- Xiao, Tianbai. 2021b. "Kinetic.jl: A Portable Finite Volume Toolbox for Scientific and Neural Computing." *Journal of Open Source Software* 6 (62): 3060.
- Xiao, Tianbai, Qingdong Cai, and Kun Xu. 2017. "A Well-Balanced Unified Gas-Kinetic Scheme for Multiscale Flow Transport Under Gravitational Field." *Journal of Computational Physics* 332: 475–491.
- Xiao, Tianbai, and Martin Frank. 2021a. "A Stochastic Kinetic Scheme for Multi-scale Flow Transport with Uncertainty Quantification." *Journal of Computational Physics* 437: 110337.
- Xiao, Tianbai, and Martin Frank. 2021b. "A Stochastic Kinetic Scheme for Multi-scale Plasma Transport with Uncertainty Quantification." *Journal of Computational Physics* 432: 110139.
- Xiao, Tianbai, Chang Liu, Kun Xu, and Qingdong Cai. 2020. "A Velocity-Space Adaptive Unified Gas Kinetic Scheme for Continuum and Rarefied Flows." *Journal of Computational Physics* 415: 109535.
- Xiao, Tianbai, Kun Xu, Qingdong Cai, and Tiezheng Qian. 2018. "An Investigation of Non-equilibrium Heat Transport in a Gas System Under External Force Field." *International Journal of Heat and Mass Transfer* 126: 362–379.
- Xiu, Dongbin, and George Em Karniadakis. 2003. "Modeling Uncertainty in Flow Simulations Via Generalized Polynomial Chaos." *Journal of Computational Physics* 187 (1): 137–167.
- Xu, Kun. 2001. "A Gas-Kinetic BGK Scheme for the Navier–Stokes Equations and Its Connection with Artificial Dissipation and Godunov Method." *Journal of Computational Physics* 171 (1): 289–335.
- Xu, Kun, and Juan-Chen Huang. 2010. "A Unified Gas-Kinetic Scheme for Continuum and Rarefied Flows." *Journal of Computational Physics* 229 (20): 7747–7764.

## Appendix

In this appendix, we provide a further validation of the current SKS. As the merit of the SKS is the coupled treatment of particle transport and collision in the evaluation of numerical flux, we compare its performance here with the numerical method proposed in the literature, which employs a purely upwind flux function (Hu and Jin 2017). Note that the motivation here is not to censure such methodology, but rather to choose a

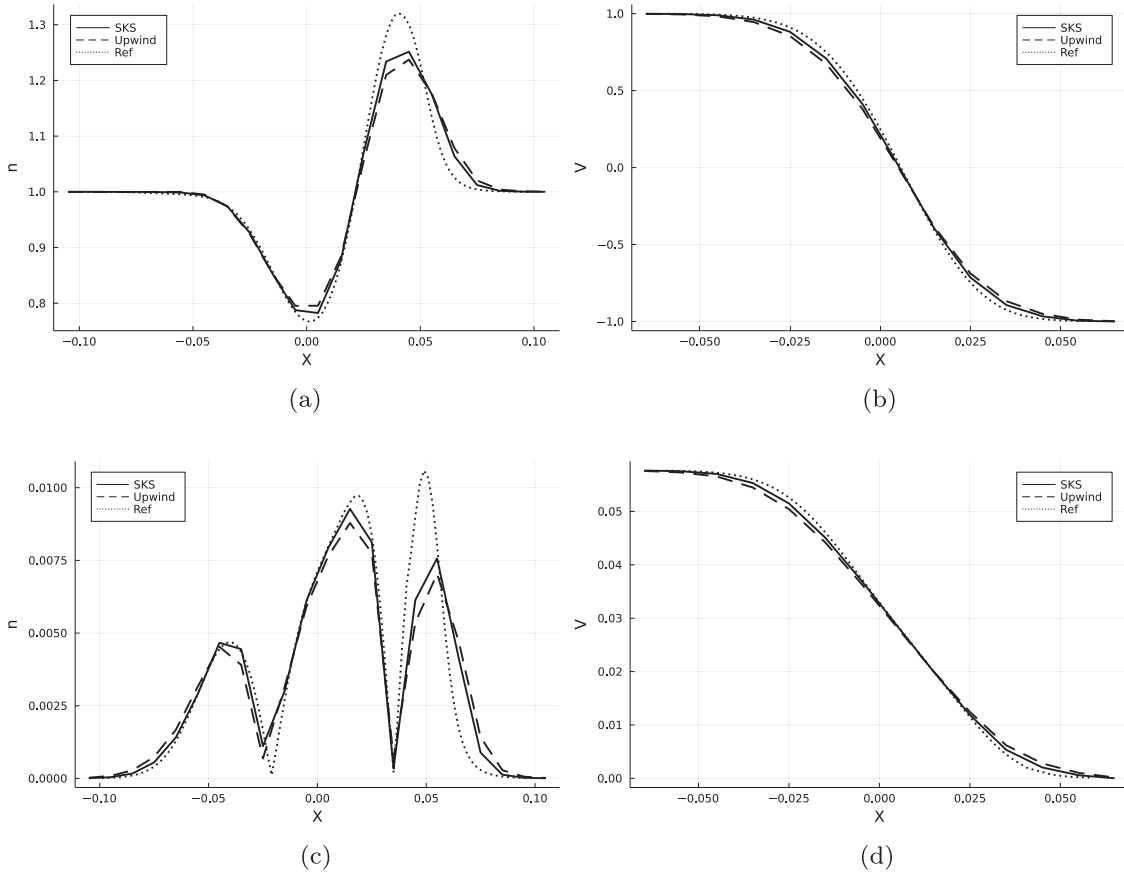


**Figure A1.** Expectation values and standard deviations of macroscopic density and  $V$ -velocity at  $t = 10\tau_0$  computed by the SKS and upwind schemes with 200 spatial cells in the shear layer problem: (a)  $\mathbb{E}(n)$ , (b)  $\mathbb{E}(V)$ , (c)  $\mathbb{S}(n)$  and (d)  $\mathbb{S}(V)$ .

widely adopted numerical scheme as benchmark to illustrate the reliability of our method for the study of multi-scale and non-equilibrium flows.

The shear layer from Section 4.3 is used as the benchmark problem. While keeping the rest computational setups, we employ a much coarser spatial grid and provide a grid-convergence test of different numerical schemes. Figures A1 and A2 show the expectation values and standard deviations of density and  $V$ -velocity with 200 cells at  $t = 10\tau_0$  and  $100\tau_0$ , and Figures A3 and A4 provide the results with 400 cells.

As can be seen, compared with method with pure upwind flux, the current SKS invariably provides the solution that are

closer to the reference solution under different numerical resolutions. Thanks to the coupling of particle transport and collision in the construction of interface distribution function, the numerical dissipation introduced in this step is of  $O(\tau)$ , where  $\tau = 1/\nu$  is the mean collision time, while the pure upwind flux introduces the numerical error of  $O(\Delta t)$ , where  $\Delta t$  is the time step or the time interval in a multi-step integration. As a result, the current method provides sharper flow structures on a relatively coarse mesh and ensures faster convergence of solutions, especially for near-continuum and long-time flow evolutions where  $t \gg \tau$ . The detailed mathematical analysis can be found in Xu (2001) and Xiao et al. (2020).

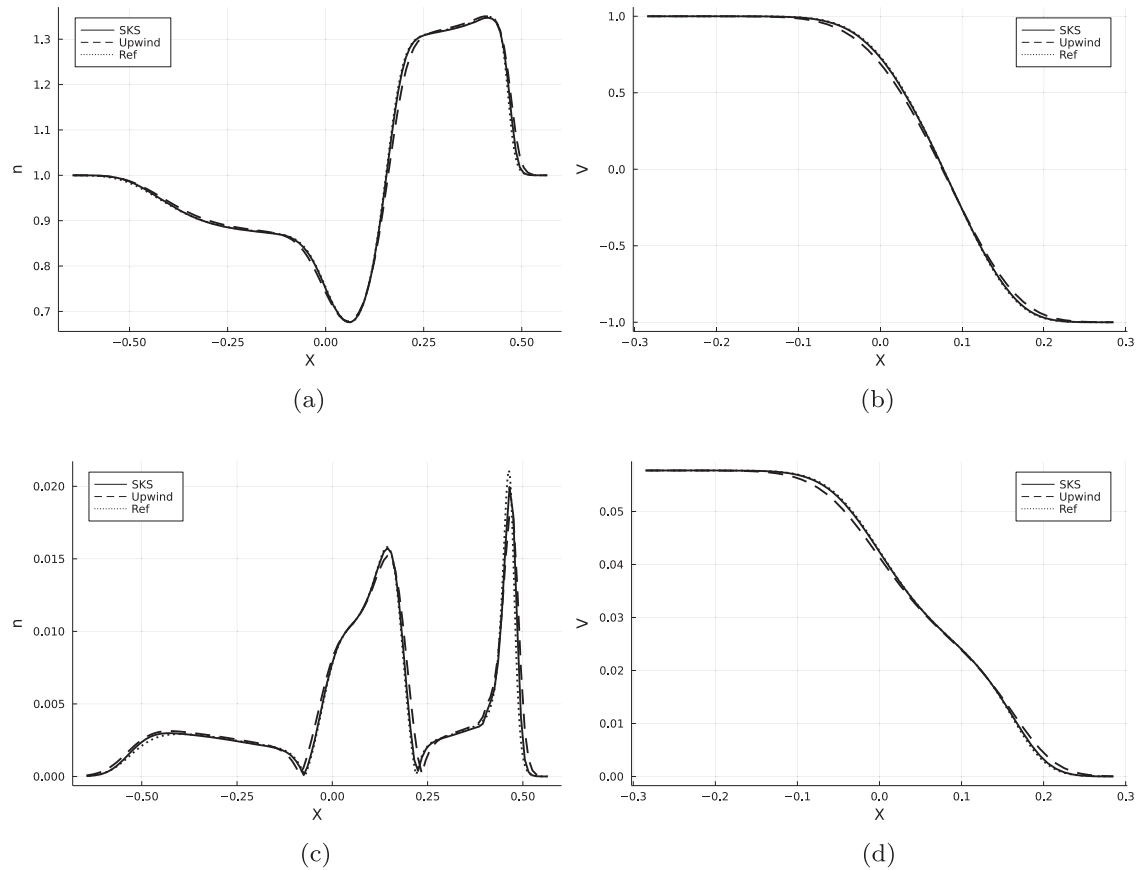


**Figure A2.** Expectation values and standard deviations of macroscopic density and  $V$ -velocity at  $t = 100\tau_0$  computed by the SKS and upwind schemes with 200 spatial cells in the shear layer problem: (a)  $\mathbb{E}(n)$ , (b)  $\mathbb{E}(V)$ , (c)  $\mathbb{S}(n)$  and (d)  $\mathbb{S}(V)$ .

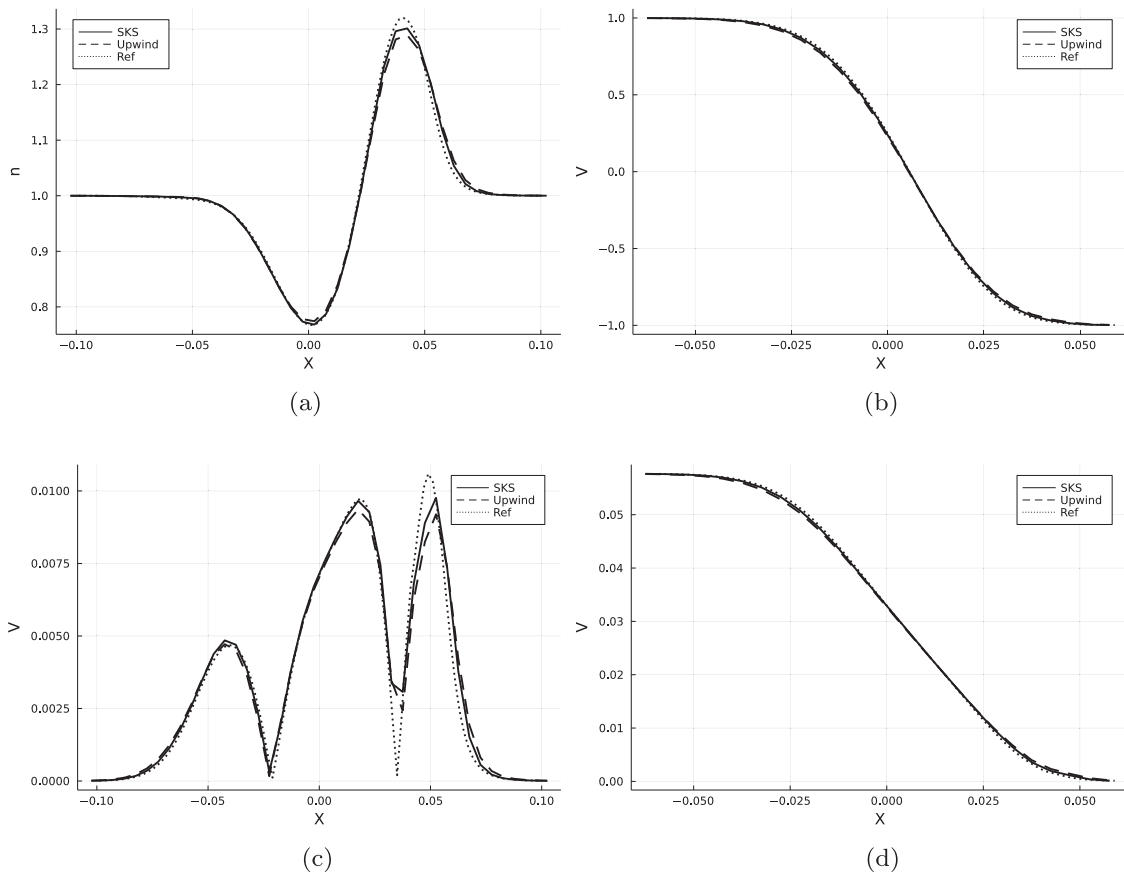


**Figure A3.** Expectation values and standard deviations of macroscopic density and  $V$ -velocity at  $t = 10\tau_0$  computed by the SKS and upwind schemes with 400 spatial cells in the shear layer problem: (a)  $\mathbb{E}(n)$ , (b)  $\mathbb{E}(V)$ , (c)  $\mathbb{S}(n)$  and (d)  $\mathbb{S}(V)$ .

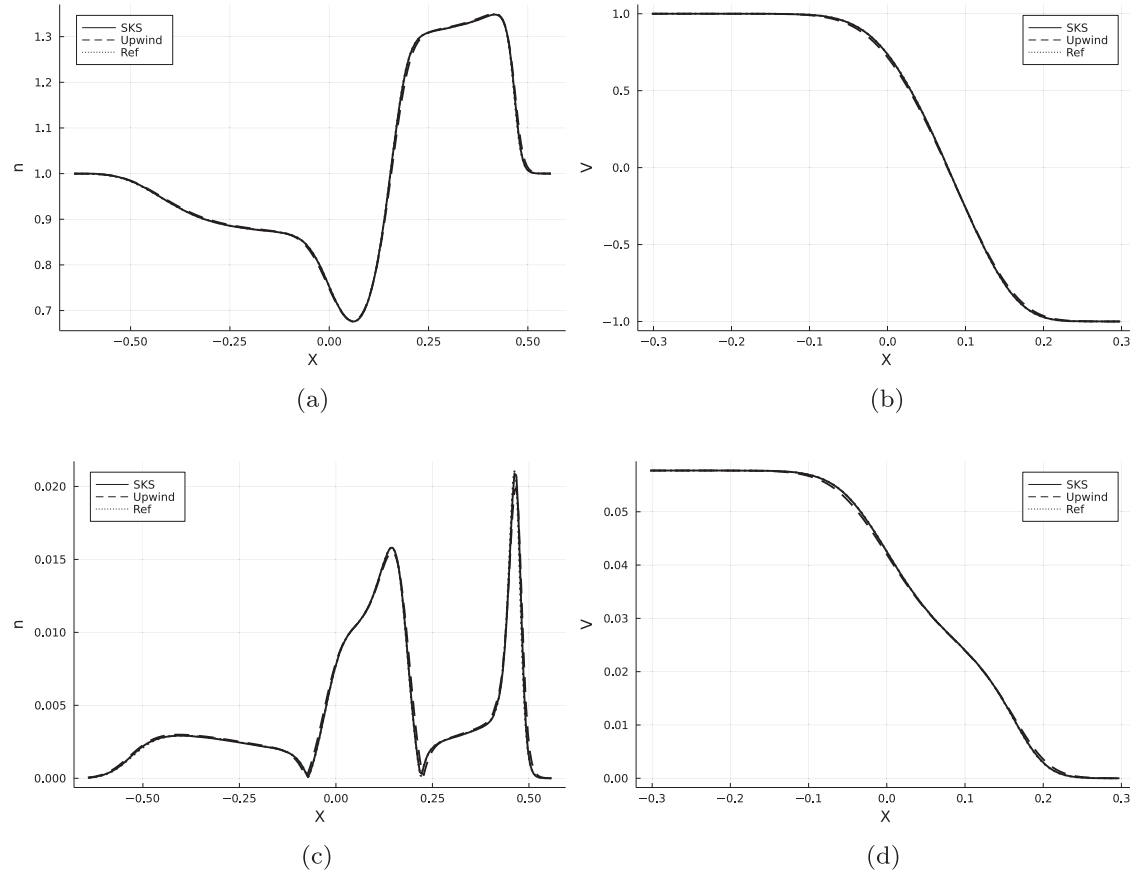


**Figure A4.** Expectation values and standard deviations of macroscopic density and  $V$ -velocity at  $t = 100\tau_0$  computed by the SKS and upwind schemes with 400 spatial cells in the shear layer problem: (a)  $\mathbb{E}(n)$ , (b)  $\mathbb{E}(V)$ , (c)  $\mathbb{S}(n)$  and (d)  $\mathbb{S}(V)$ .